PHYSICAL REVIEW B **80**, 045326 (2009)

Artificial quantum-dot helium molecules: Electronic spectra, spin structures, and Heisenberg clusters

Ying Li, Constantine Yannouleas,* and Uzi Landman†
School of Physics, Georgia Institute of Technology, Atlanta, Georgia 30332-0430, USA

(Received 30 January 2009; revised manuscript received 6 May 2009; published 30 July 2009)

Energy spectra and spin configurations of a system of $N=4$ electrons in lateral double quantum dots (quantum dot helium molecules) are investigated using exact diagonalization (EXD), as a function of interdot separation, applied magnetic field (B), and strength of interelectron repulsion. As a function of the magnetic field, the energy spectra exhibit a low-energy band consisting of a group of six states, with the number six being a consequence of the conservation of the total spin and the ensuing spin degeneracies for four electrons. The energies of the six states appear to cross at a single value of the magnetic field, and with increasing Coulomb repulsion they tend to become degenerate, with a well-defined energy gap separating them from the higher-in-energy excited states. The appearance of the low-energy band is a consequence of the formation of a Wigner supermolecule, with the four electrons (two in each dot) being localized at the vertices of a rectangle. Using spin-resolved pair-correlation distributions, a method for mapping the complicated EXD many-body wave functions onto simpler spin functions associated with a system of four localized spins is introduced. Detailed interpretation of the EXD spin functions and EXD spectra associated with the low-energy band via a four-site Heisenberg cluster (with B-dependent exchange integrals) is demonstrated. Aspects of spin entanglement, referring to the well-known N-qubit Dicke states, are also discussed.

DOI: 10.1103/PhysRevB.80.045326 PACS number(s): 73.21.La, 31.15.V−, 03.67.Mn, 03.65.Ud

I. INTRODUCTION

The field of two-dimensional (2D) semiconductor quantum dots (QDs) has witnessed rapid expansion in the last several years, both experimentally[1,2] and theoretically.[3–5] Along with fundamental interest in the properties of such systems, and as a test ground for highly correlated electrons, a major motivation for these growing endeavors has been the promising outlook and potential of quantum dots concerning the implementation of solid-state quantum computing and quantum information devices.[6–10] To this effect highly precise control of the space and spin degrees of freedom of a small number N of confined electrons (down to an empty[11–13] QD) needs to be achieved, and experimentally this was demonstrated recently for two electrons in a lateral double quantum-dot molecule (see Ref. 2 and references therein). From the theoretical standpoint, high-level computational methods that reach beyond the level of mean-field approximation are needed,[5] with the ability to provide solutions that preserve all the symmetries of the many-body Hamiltonian, and in particular those associated with the total spin. In this context, electrons in quantum dots exhibit localization in space and formation of Wigner molecules (see, e.g., Ref. 5). When the spin degree of freedom is considered, such Wigner molecules may be viewed as finite Heisenberg spin clusters[14,15] whose quantum behavior (due to finite-size fluctuations and correlation effects) differs drastically from the behavior expected from magnetic systems in the thermodynamic limit.[14,16]

There is an abundance of experimental and theoretical publications concerning *circular single* quantum dots with a small number of electrons.[1,3,5,17–19] In this paper, we use exact diagonalization[4,5,18] (EXD) to investigate the properties of *lateral double quantum dots* (DQDs) containing four electrons. DQDs are referred to also as artificial molecules. Specifically in the case of four electrons they can be viewed as artificial *quantum-dot helium molecules*.[20] DQDs containing two electrons have been already studied extensively both experimentally[2] and theoretically.[5,21,22] However, experimental studies of DQDs with more than two electrons are relatively few.[23,24] We are aware of a single theoretical EXD study of a lateral DQD with three electrons[25] and another one of two laterally coupled quantum rings with three electrons.[26]

In light of the different quantum behavior discovered in our investigations (compared to circular QDs with regard to the spectra, spin structures, and analogies with Heisenberg clusters), we hope that the present work would serve as an impetus for further experimental studies on lateral DQDs. In particular, as a function of the magnetic field, we find that (1) a low-energy band of six states develops as the strength of the Coulomb repulsion increases, separated by an energy gap from the other excited states, and (2) all six states appear to "cross" at a single value of the magnetic field. The crossing point gets sharper for larger interdot distances. We find that the specific number of crossing states (six) derives from the spin degeneracies and multiplicities expressed by the branching diagram.[27]

The formation of the low-energy band is a consequence of the localization of the four electrons within each dot (with two electrons in each dot). This localization leads to formation (with increasing strength of the Coulomb repulsion) of a Wigner supermolecule[28] with the four localized electrons (two in each dot) being located at the corners of a rectangular parallelogram (RP). Using the spin-resolved pair-correlation functions, we show how to map the EXD many-body wave functions onto the spin functions associated with the four localized spins. This mapping leads us naturally to study analogies with finite systems described by a model Heisenberg Hamiltonian (often referred to as finite Heisenberg clusters). Specifically, we provide a detailed interpretation of the EXD spin functions and EXD spectra associated with the low-energy band via a four-site finite Heisenberg cluster characterized by two (intradot and interdot) exchange integrals.

More importantly, our EXD calculations exhibit a prominent oscillatory magnetic-field dependence of the two exchange integrals entering in this four-site Heisenberg Hamiltonian. Such strong B dependence of the exchange integrals has been found in previous theoretical studies in the simpler case of two electrons in double quantum dots,[7,21,22,29,30] as well as in anisotropic single quantum dots.[31,32] The B dependence in the case of two electrons in quantum dots has also been observed experimentally.[31–33] Following an earlier proposal,[7] the B dependence of the exchange integral for the two-electron case has developed into a central theme in experimental efforts aiming at solid-state implementation of quantum computing.[2,24] Our EXD results in this paper extend the B dependence of the exchange integrals to larger numbers ($N>2$) of electrons in quantum-dot molecules.

We further discuss that the determination of the equivalent spin functions enables consideration of aspects of entanglement regarding the EXD solutions. In particular, we show that the formation of Wigner supermolecules leads to strongly entangled states known in the literature of quantum information as N-qubit Dicke states.[34–37]

We finally mention that the trends in the excitation spectra (e.g., formation of a low-energy band) and entanglement characteristics (e.g., mapping to spin functions of localized electrons) found in the case of double quantum dots have many analogies with those found in other deformed configurations, and in particular single anisotropic quantum dots; see, e.g., the case of three electrons in Ref. 38.

The plan of the paper is as follows:

(i) Sec. II describes the two-dimensional two-center-oscillator (TCO) external confining potential that models the double quantum dot.

(ii) Section III reviews the many-body Hamiltonian and the exact-diagonalization method as implemented in this paper.

(iii) Section IV outlines some theoretical background regarding the general form of four-electron spin eigenfunctions and the branching diagram (which describes the breakdown of spin multiplicities for given N).

(iv) Section V describes our numerical results from the exact diagonalization, that is, the EXD spectra, the electron densities, and the spin-resolved conditional probability distributions (CPDs).

(v) Section VI provides an interpretation of the numerical EXD results for the six-state lower-energy band with the help of a four-site Heisenberg Hamiltonian.

(vi) Section VII contains two parts which discuss (a) the importance of B-dependent exchange integrals in the Heisenberg Hamiltonian and (b) the aspects of entanglement exhibited by the EXD wave functions.

(vii) Section VIII offers a summary.

(viii) Finally, the Appendix describes the single-particle spectrum of the two-center oscillator (when the two-body Coulomb interaction is omitted; noninteracting model).

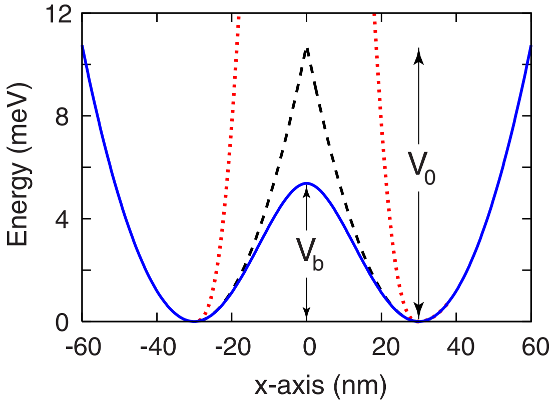

FIG. 1. (Color online) Cuts at $y=0$ of the two-center-oscillator confining potential along the x axis for an interdot separation of $d=60$ nm. Solid line (blue): double-oscillator confining potential with a smooth connecting neck specified by $\epsilon^b=V_b/V_0=0.5$. Dashed line (black): double-oscillator confining potential without a smooth connecting neck. Dotted line (red): double-oscillator confining potential with a smooth connecting neck specified by $\epsilon^b=6$. The remaining parameters are $\hbar\omega_{x1}=\hbar\omega_{x2}=\hbar\omega_0=5.1$ meV, $m^*=0.070m_e$, $h_1=h_2=0$, $V_{01}=V_{02}=V_0$, and $\epsilon_1^b=\epsilon_2^b=\epsilon^b$.

II. TWO-DIMENSIONAL TWO-CENTER-OSCILLATOR CONFINING POTENTIAL

In the two-dimensional two-center-oscillator, the single-particle levels associated with the confining potential of the artificial molecule are determined by the single-particle Hamiltonian[39]

$$H=T+\frac{1}{2}m^*\omega_y^2y^2+\frac{1}{2}m^*\omega_{xk}^2x_k'^2+V_{\mathrm{neck}}(x)+h_k+\frac{g^*\mu_B}{\hbar}\mathbf{B}\cdot\mathbf{s}, \tag{1}$$

where $x_k'=x-x_k$ with $k=1$ for $x<0$ (left) and $k=2$ for $x>0$ (right), and the h_k's control the relative well depth, thus allowing studies of hetero-QDMs. y denotes the coordinate perpendicular to the interdot axis (x). $T=(\mathbf{p}-e\mathbf{A}/c)^2/2m^*$, with $\mathbf{A}=0.5(-By,Bx,0)$, and the last term in Eq. (1) is the Zeeman interaction with g^* being the effective g factor, μ_B the Bohr magneton, and $\mathbf{s}$ the spin of an individual electron. The most general shapes described by H are two semiellipses connected by a smooth neck $V_{\mathrm{neck}}(x)$ (see solid line in Fig. 1). $x_1<0$ and $x_2>0$ are the centers of these semiellipses, $d=x_2-x_1$ is the interdot distance, and m^* is the effective electron mass.

For the smooth connecting neck, we use $V_{\mathrm{neck}}(x)=\frac{1}{2}m^*\omega_{xk}^2[\mathcal{C}_kx_k'^3+\mathcal{D}_kx_k'^4]\theta(|x|-|x_k|)$, where $\theta(u)=0$ for $u>0$ and $\theta(u)=1$ for $u<0$. The four constants $\mathcal{C}_k$ and $\mathcal{D}_k$ can be expressed via two parameters, as follows: $\mathcal{C}_k=(2-4\epsilon_k^b)/x_k$ and $\mathcal{D}_k=(1-3\epsilon_k^b)/x_k^2$, where the barrier-control parameters $\epsilon_k^b=(V_b-h_k)/V_{0k}$ are related to the actual (controllable) height of the bare interdot barrier (V_b) between the two QDs, and $V_{0k}=m^*\omega_{xk}^2x_k^2/2$ (for $h_1=h_2$, $V_{01}=V_{02}=V_0$).

The single-particle levels of H, including an external perpendicular magnetic field B, are obtained by numerical diagonalization in a (variable-with-separation) basis consisting of the eigenstates of the auxiliary (zero-field) Hamiltonian:

$$H_0 = \frac{\mathbf{p}^2}{2m^*} + \frac{1}{2}m^*\omega_y^2 y^2 + \frac{1}{2}m^*\omega_{xk}^2 x_k'^2 + h_k. \tag{2}$$

The eigenvalue problem associated with the auxiliary Hamiltonian [Eq. (2)] is separable in x and y, i.e., the wave functions are written as

$$\varphi_i(x,y) = X_\mu(x)Y_n(y), \tag{3}$$

with $i \equiv \{\mu, n\}$, $i=1,2,\ldots,K$.

The $Y_n(y)$ are the eigenfunctions of a one-dimensional oscillator, and the $X_\mu(x \leq 0)$ or $X_\mu(x>0)$ can be expressed through the parabolic cylinder functions[40,41] $U[\gamma_k, (-1)^k\xi_k]$, where $\xi_k = x_k'\sqrt{2m^*\omega_{xk}/\hbar}$, $\gamma_k = (-E_x + h_k)/(\hbar\omega_{xk})$, and $E_x = (\mu + 0.5)\hbar\omega_{x1} + h_1$ denotes the x eigenvalues. The matching conditions at $x=0$ for the left and right domains yield the x eigenvalues and the eigenfunctions $X_\mu(x)$. The n indices are integers. The number of μ indices is finite; however, they are in general real numbers.

In the Appendix, we discuss briefly the energy spectra associated with the single-particle states of the two-center oscillator Hamiltonian given by Eq. (1). We follow there the notation presented first in Ref. 42. For further details, see Ref. 43.

In this paper, we will limit ourselves to QDMs with $x_2 = -x_1$ and $\hbar\omega_y = \hbar\omega_{x1} = \hbar\omega_{x2} = \hbar\omega_0$. However, in several instances we will compare with the case of a single elliptic QD where $x_2 = -x_1 = 0$ and $\hbar\omega_y \neq \hbar\omega_x = \hbar\omega_{x1} = \hbar\omega_{x2}$. In all cases, we will use $\hbar\omega_0 = 5.1$ meV, $m^* = 0.070m_e$ (this effective-mass value corresponds to GaAs), and $K=50$ (which guarantees numerical convergence[44]).

III. MANY-BODY HAMILTONIAN AND THE EXACT DIAGONALIZATION METHOD

The many-body Hamiltonian $\mathcal{H}$ for a dimeric QDM comprising N electrons can be expressed as a sum of the single-particle part $H(i)$ defined in Eq. (1) and the two-particle interelectron Coulomb repulsion,

$$\mathcal{H} = \sum_{i=1}^{N} H(i) + \sum_{i=1}^{N}\sum_{j>i}^{N} \frac{e^2}{\kappa r_{ij}}, \tag{4}$$

where κ is the dielectric constant and r_{ij} denotes the relative distance between the i and j electrons.

As we mentioned in the introduction, we will use the method of exact diagonalization for determining[43] the solution of the many-body problem specified by Hamiltonian (4).

In the EXD method, one writes the many-body wave function $\Phi_N^{\mathrm{EXD}}(\mathbf{r}_1, \mathbf{r}_2, \ldots, \mathbf{r}_N)$ as a linear superposition of Slater determinants $\Psi^N(\mathbf{r}_1, \mathbf{r}_2, \ldots, \mathbf{r}_N)$ that span the many-body Hilbert space and are constructed out of the single-particle *spin-orbitals*

$$\chi_j(x,y) = \varphi_j(x,y)\alpha, \quad \text{if} \quad 1 \leq j \leq K, \tag{5}$$

and

$$\chi_j(x,y) = \varphi_{j-K}(x,y)\beta, \quad \text{if} \quad K < j \leq 2K, \tag{6}$$

where $\alpha(\beta)$ denote up (down) spins. Namely

$$\Phi_{N,q}^{\mathrm{EXD}}(\mathbf{r}_1, \ldots, \mathbf{r}_N) = \sum_I C_I^q \Psi_I^N(\mathbf{r}_1, \ldots, \mathbf{r}_N), \tag{7}$$

where

$$\Psi_I^N = \frac{1}{\sqrt{N!}}\begin{vmatrix} \chi_{j_1}(\mathbf{r}_1) & \ldots & \chi_{j_N}(\mathbf{r}_1) \\ \vdots & \ddots & \vdots \\ \chi_{j_1}(\mathbf{r}_N) & \ldots & \chi_{j_N}(\mathbf{r}_N) \end{vmatrix}, \tag{8}$$

and the master index I counts the number of arrangements $\{j_1, j_2, \ldots, j_N\}$ under the restriction that $1 \leq j_1 < j_2 < \ldots < j_N \leq 2K$. $q=1,2,\ldots$ counts the excitation spectrum, with $q=1$ corresponding to the ground state.

The exact diagonalization of the many-body Schrödinger equation

$$\mathcal{H}\Phi_{N,q}^{\mathrm{EXD}} = E_{N,q}^{\mathrm{EXD}}\Phi_{N,q}^{\mathrm{EXD}} \tag{9}$$

transforms into a matrix diagonalization problem, which yields the coefficients C_I^q and the EXD eigenenergies $E_{N,q}^{\mathrm{EXD}}$. Because the resulting matrix is sparse, we implement its numerical diagonalization employing the well-known ARPACK solver.[45]

The matrix elements $\langle \Psi_N^I | \mathcal{H} | \Psi_N^J \rangle$ between the basis determinants [see Eq. (8)] are calculated using the Slater rules.[46] Naturally, an important ingredient in this respect are the two-body matrix elements of the Coulomb interaction,

$$\frac{e^2}{\kappa}\int_{-\infty}^{\infty}\int_{-\infty}^{\infty} d\mathbf{r}_1 d\mathbf{r}_2 \varphi_i^*(\mathbf{r}_1)\varphi_j^*(\mathbf{r}_2)\frac{1}{|\mathbf{r}_1 - \mathbf{r}_2|}\varphi_k(\mathbf{r}_1)\varphi_l(\mathbf{r}_2), \tag{10}$$

in the basis formed out of the single-particle spatial orbitals $\varphi_i(\mathbf{r})$, $i=1,2,\ldots,K$ [Eq. (3)]. In our approach, these matrix elements are determined numerically and stored separately. Varying the dielectric constant κ and/or the interdot-barrier parameter ϵ^b does not require a recalculation of the Coulomb-interaction matrix elements as long as the remaining parameters are kept the same.

The Slater determinants Ψ_I^N [see Eq. (8)] conserve the third projection S_z, but not the square $\hat{\mathbf{S}}^2$ of the total spin. However, because $\hat{\mathbf{S}}^2$ commutes with the many-body Hamiltonian, the EXD solutions are automatically eigenstates of $\hat{\mathbf{S}}^2$ with eigenvalues $S(S+1)$. After the diagonalization, these eigenvalues are determined by applying $\hat{\mathbf{S}}^2$ onto $\Phi_{N,q}^{\mathrm{EXD}}$ and using the relation

$$\hat{\mathbf{S}}^2\Psi_I^N = \left[(N_\alpha - N_\beta)^2/4 + N/2 + \sum_{i<j}\varpi_{ij}\right]\Psi_I^N, \tag{11}$$

where the operator ϖ_{ij} interchanges the spins of electrons i and j provided that their spins are different; N_α and N_β denote the number of spin-up and spin-down electrons, respectively.

Of great help in reducing the size of the matrices to be diagonalized is the fact that the parity (with respect to the origin) of the EXD many-body wave function is a good quantum number for all values of the magnetic field when

$h_1 = h_2$. Specifically, the xy-parity operator associated with reflections about the origin of the axes is defined as

$$\hat{\mathcal{P}}_{xy}\Phi_{N,q}^{\mathrm{EXD}}(\mathbf{r}_1,\mathbf{r}_2,\mathbf{r}_3,\mathbf{r}_4) = \Phi_{N,q}^{\mathrm{EXD}}(-\mathbf{r}_1,-\mathbf{r}_2,-\mathbf{r}_3,-\mathbf{r}_4) \quad (12)$$

and has eigenvalues ± 1.

One can also consider partial parity operators $\hat{\mathcal{P}}_x$ and $\hat{\mathcal{P}}_y$ associated solely with reflections about the x and y axes, respectively; of course $\hat{\mathcal{P}}_{xy} = \hat{\mathcal{P}}_x\hat{\mathcal{P}}_y$. We note that unlike $\hat{\mathcal{P}}_{xy}$, the partial parities $\hat{\mathcal{P}}_x$ and $\hat{\mathcal{P}}_y$ are conserved only for zero magnetic fields ($B=0$). With the two-center oscillator *Cartesian* basis that we use [see Eq. (3)], it is easy to calculate the parity eigenvalues for the Slater determinants, Eq. (8), that span the many-body Hilbert space. Because $X_\mu(x)$ and $Y_n(y)$ conserve the partial $\hat{\mathcal{P}}_x$ and $\hat{\mathcal{P}}_y$ parities, respectively, one finds

$$\hat{\mathcal{P}}_{xy}\Psi_I^N = (-)^{\sum_{i=1}^{4} m_i + n_i}\Psi_I^N, \quad (13)$$

where m_i and n_i count the number of single-particle states associated with the bare two-center oscillator [see the auxiliary Hamiltonian H_0 in Eq. (2)] along the x axis and the simple oscillator along the y direction (with the assumption that the lowest states have $m=0$ and $n=0$, since they are even states). We note again that the index μ in Eq. (3) is not an integer in general, while m here is indeed an integer (since it counts the number of single-particle states along the x direction).

IV. MANY-BODY SPIN EIGENFUNCTIONS

For completeness and for the reader's convenience, we outline in this section several well established (but often not well known) properties of the many-body spin eigenfunctions which are useful for analyzing the trends and behavior of the spin multiplicities exhibited by the EXD wave functions for $N=4$ electrons. We stress here that the ability to describe spin multiplicities is an advantage of the EXD method compared to the more familiar spin-density functional approaches whose single-determinantal wave functions preserve only the third projection S_z of the total spin, and thus are subject to "spin contamination" errors. As we will discuss below, the spin multiplicities of the EXD wave functions lead naturally to formation of highly entangled Dicke states[34–37] and most importantly to analogies with finite Heisenberg clusters.[14,15]

A basic property of spin eigenfunctions is that they exhibit degeneracies for $N>2$, i.e., there may be more than one linearly independent (and orthogonal) spin functions that are simultaneous eigenstates of both $\hat{\mathbf{S}}^2$ and S_z. These degeneracies are usually visualized by means of the *branching diagram*[27] displayed in Fig. 2. The axes in this plot describe the number N of fermions (horizontal axis) and the quantum number S of the total spin (vertical axis). At each point (N,S), a circle is drawn containing the number $g(N,S)$ which gives the degeneracy of spin states. It is found[27] that

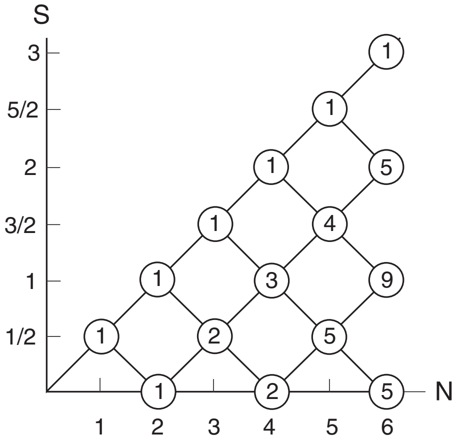

FIG. 2. The branching diagram for the spin degeneracies. The total-spin quantum number S is given on the vertical axis, and the number of particles, N, on the horizontal one. The numbers inside the circles give the number, $g(N,S)$, of linear independent (and orthogonal) spin functions for the corresponding values of N and S.

$$g(N,S) = \binom{N}{N/2 - S} - \binom{N}{N/2 - S - 1}. \quad (14)$$

Specifically for $N=4$ particles, there is one spin eigenfunction with $S=2$, three with $S=1$, and two with $S=0$. In general the spin part of the EXD wave functions involves a linear superposition over all the degenerate spin eigenfunctions for a given S.

For a small number of particles, one can find compact expressions that encompass all possible superpositions. For example, for $N=4$ and $S=0$, $S_z=0$ one has[47]

$$\begin{aligned}\mathcal{X}_{00} = {} & \sqrt{\frac{1}{3}}\sin\theta|\uparrow\uparrow\downarrow\downarrow\rangle + \left(\frac{1}{2}\cos\theta - \sqrt{\frac{1}{12}}\sin\theta\right)|\uparrow\downarrow\uparrow\downarrow\rangle \\ & - \left(\frac{1}{2}\cos\theta + \sqrt{\frac{1}{12}}\sin\theta\right)|\uparrow\downarrow\downarrow\uparrow\rangle \\ & - \left(\frac{1}{2}\cos\theta + \sqrt{\frac{1}{12}}\sin\theta\right)|\downarrow\uparrow\uparrow\downarrow\rangle \\ & + \left(\frac{1}{2}\cos\theta - \sqrt{\frac{1}{12}}\sin\theta\right)|\downarrow\uparrow\downarrow\uparrow\rangle + \sqrt{\frac{1}{3}}\sin\theta|\downarrow\downarrow\uparrow\uparrow\rangle,\end{aligned} \quad (15)$$

where the parameter θ satisfies $-\pi/2 \le \theta \le \pi/2$ and is chosen such that $\theta=0$ corresponds to the spin function with intermediate two-electron spin $S_{12}=0$ and three-electron spin $S_{123}=1/2$; whereas $\theta=\pm\pi/2$ corresponds to the one with intermediate spins $S_{12}=1$ and $S_{123}=1/2$.

For $N=4$ and $S=1$, $S_z=0$ one has

$$\mathcal{X}_{10}=\left(\sqrt{\frac{1}{6}}\sin\theta\sin\varphi-\sqrt{\frac{1}{12}}\sin\theta\cos\varphi-\frac{1}{2}\cos\theta\right)|\downarrow\uparrow\uparrow\downarrow\rangle+\left(\sqrt{\frac{1}{6}}\sin\theta\sin\varphi-\sqrt{\frac{1}{12}}\sin\theta\cos\varphi+\frac{1}{2}\cos\theta\right)|\uparrow\downarrow\uparrow\downarrow\rangle$$
$$+\left(\sqrt{\frac{1}{12}}\sin\theta\cos\varphi-\sqrt{\frac{1}{6}}\sin\theta\sin\varphi-\frac{1}{2}\cos\theta\right)|\downarrow\uparrow\downarrow\uparrow\rangle+\left(\sqrt{\frac{1}{12}}\sin\theta\cos\varphi-\sqrt{\frac{1}{6}}\sin\theta\sin\varphi+\frac{1}{2}\cos\theta\right)|\uparrow\downarrow\downarrow\uparrow\rangle$$
$$+\left(\sqrt{\frac{1}{6}}\sin\theta\sin\varphi+\sqrt{\frac{1}{3}}\sin\theta\cos\varphi\right)|\uparrow\uparrow\downarrow\downarrow\rangle-\left(\sqrt{\frac{1}{6}}\sin\theta\sin\varphi+\sqrt{\frac{1}{3}}\sin\theta\cos\varphi\right)|\downarrow\downarrow\uparrow\uparrow\rangle, \tag{16}$$

where the parameters θ and φ satisfy $-\pi/2\leq\theta\leq\pi/2$ and $-\pi/2\leq\varphi\leq\pi/2$. Three independent spin functions with definite intermediate two-electron, S_{12}, and three-electron, S_{123}, spin values correspond to the θ and φ values as follows: for $S_{12}=0$ and $S_{123}=1/2$, $\theta=0$; for $S_{12}=1$ and $S_{123}=1/2$, $\theta=\pm\pi/2$ and $\varphi=0$; and for $S_{12}=1$ and $S_{123}=3/2$, $\theta=\pm\pi/2$ and $\varphi=\pm\pi/2$.

Finally, for $N=4$ and $S=2$, $S_z=0$ (maximum polarization) case, one has

$$\mathcal{X}_{20}=\frac{|\downarrow\downarrow\uparrow\uparrow\rangle+|\downarrow\uparrow\downarrow\uparrow\rangle+|\downarrow\uparrow\uparrow\downarrow\rangle+|\uparrow\downarrow\downarrow\uparrow\rangle+|\uparrow\downarrow\uparrow\downarrow\rangle+|\uparrow\uparrow\downarrow\downarrow\rangle}{\sqrt{6}}. \tag{17}$$

V. EXACT-DIAGONALIZATION RESULTS

A. Energy spectra

The excitation spectra as a function of the applied magnetic field for four electrons in a double QD with interdot distance $d=2x_2=-2x_1=30$ nm and no voltage bias between the dots [$h_1=h_2=0$, see Eq. (1)] are plotted for three different values of the interelectron repulsion strength, i.e., weak [$\kappa=12.5$ (GaAs); see Fig. 3(a)], intermediate [$\kappa=6$; see Fig. 3(b)], and strong [$\kappa=2$; see Fig. 3(c)] Coulomb repulsion. The interdot barrier parameter was taken as $\epsilon^b=0.5$ (because $h_1=h_2=0$, one has $\epsilon_1^b=\epsilon_2^b=\epsilon^b$; see Sec. II for the definitions). In all cases, we calculated the eight lowest energy levels.

We observe that the lowest six levels form a band that separates from the rest of the spectrum through the opening of a gap. This happens already at a relatively weak interelectron repulsion and it is well developed for the intermediate case ($\kappa=6$). It is of interest to note that the number of levels in the band (six) coincides with the total number of spin eigenfunctions for $N=4$ fermions, as can be seen from the branching diagram displaying the spin degeneracies. In particular, there is one level with total spin $S=2$ (and parity $\mathcal{P}_{xy}=1$), three levels with total spin $S=1$ (two with $\mathcal{P}_{xy}=1$ and one with $\mathcal{P}_{xy}=-1$), and two levels with total spin $S=0$ (one with $\mathcal{P}_{xy}=1$ and the second with $\mathcal{P}_{xy}=-1$). All these six levels approximately cross at one point[48] situated at about $B\approx3.5$ T for $\kappa=12.5$, $B\approx2.2$ T for $\kappa=6$, and $B\approx1.1$ T for $\kappa=2$.

The trends associated with the opening of a gap and the formation of a six-state low band appear further reinforced for the larger interdot distance of $d=60$ nm (displayed in Fig. 4 for the three values of the dielectric constant $\kappa=12.5$, 6, and 2, respectively). It is remarkable that the six lower curves cross now at a sharply defined point[48] (situated at $B\approx3.3$ T for $\kappa=12.5$, $B\approx2.1$ T for $\kappa=6$, and $B\approx1.0$ T for $\kappa=2$). The six curves demonstrate additional near degeneracies regrouping approximately to three curves before and after the crossing point, which results in a remarkable simplification of the spectrum.

For strong repulsion ($\kappa=2$), all six states in the low band are almost degenerate for both distances [$d=30$ nm; see Fig. 3(c) and $d=60$ nm; see Fig. 4(c)]. This is a consequence of the formation of a near-rigid Wigner molecule (WM) with strongly localized electrons. Namely, the overlaps between the orbitals of localized electrons are very small (see, e.g., Ref. 28), yielding small exchange contributions in the total energies,[29] and thus all six possible spin multiplicities tend to become degenerate in energy. Furthermore the physical picture of a near-rigid Wigner molecule suggests that the energy gap to the next group of states corresponds to excitation of the lowest stretching vibrational mode of the four-electron molecule.

Since the main panels in Figs. 3 and 4 display only the four lowest-in-energy states with positive parity and the four corresponding states with negative parity, one needs a larger part of the spectrum to ascertain whether higher bands are formed. To this end, the inset in Fig. 4(c) displays the 12 lowest-in-energy curves with $P_{xy}=1$ and the ten corresponding curves with $P_{xy}=-1$. In addition to the six-state low band, the inset indicates formation of a higher band comprising a total of 12 states (not labeled); however, a detailed study of this higher band falls outside the scope of the present paper.

It is natural to anticipate at this point that the above behavior of the low-energy EXD spectra at low B can be generalized to an arbitrary number of electrons N in a double QD. Namely, as the strength of the interelectron interaction increases, a low-energy band comprising all possible spin multiplicities will form and it will become progressively well separated by an energy gap from the higher excitations. For example, for $N=6$, an inspection of the branching diagram in Fig. 2 leads us to the prediction that there will be 20 states in this low-energy band. A similar behavior emerges also in the case of a *single*, but strongly *anisotropic* quantum dot; indeed a low-energy band of three states (see the branching diagram in Fig. 2) has been found for $N=3$ electrons in Ref. 38.

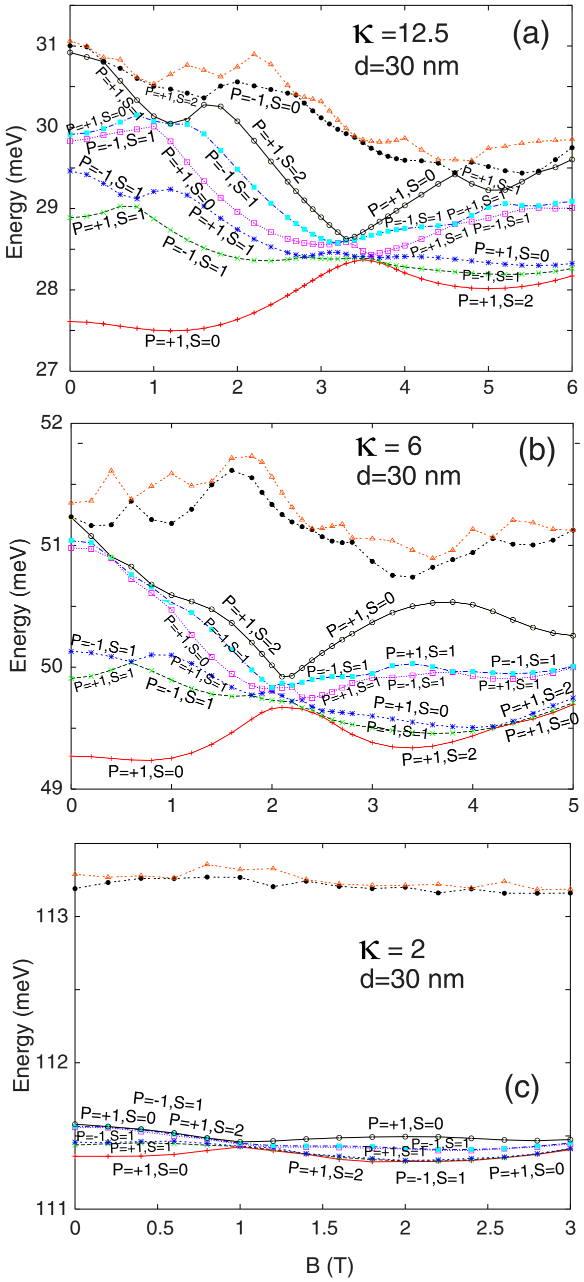

FIG. 3. (Color online) Energy spectra (as a function of the magnetic field B) for $N=4$ electrons in a double quantum dot with interdot separation $d=30$ nm. (a) $\kappa=12.5$ corresponds to GaAs. (b) $\kappa=6$. (c) $\kappa=2$. The Zeeman term was neglected and thus all states with the same total spin S and different spin projections S_z are degenerate. Remaining parameters: $\epsilon^b=0.5$, $\hbar\omega_0=5.1$ meV, $m^*=0.07m_e$, and $h_1=h_2=0$. For all figures in this paper, $\hbar\omega_0$, m^*, and $h_1=h_2$ are the same. Energies are referenced to $N\hbar\sqrt{\omega_0^2+\omega_c^2/4}$, where $\omega_c=eB/(m^*c)$ is the cyclotron frequency.

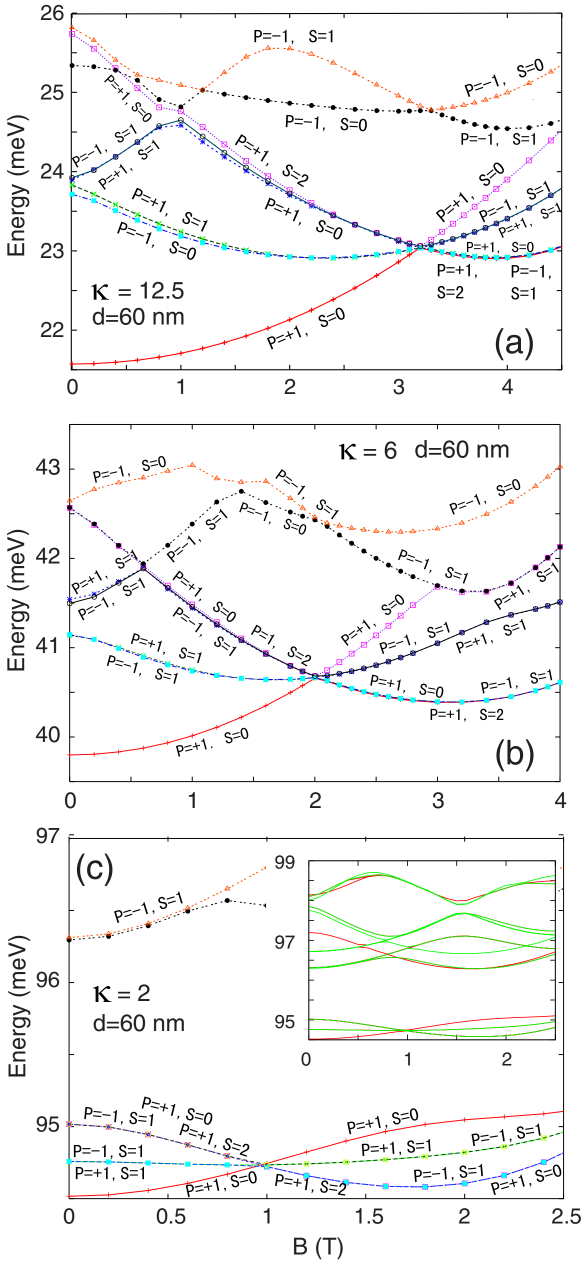

FIG. 4. (Color online) Energy spectra (as a function of the magnetic field B) for $N=4$ electrons in a double quantum dot with interdot separation $d=60$ nm. (a) $\kappa=12.5$ (weak interelectron repulsion) corresponds to GaAs. (b) $\kappa=6$. (c) $\kappa=2$. The interdot barrier corresponds to $\epsilon^b=0.5$. The inset in (c) displays all the lowest 12 $P_{xy}=1$ and the lowest 10 $P_{xy}=-1$ energies, and it demonstrates a trend toward formation of higher bands. Energies are referenced to $N\hbar\sqrt{\omega_0^2+\omega_c^2/4}$, where $\omega_c=eB/(m^*c)$ is the cyclotron frequency.

It is of interest to contrast the above behavior of the excitation spectra in a double QD with that of an N-electron circular dot. Specifically, in the circular QD, large interelectron repulsion leads to formation of a near-rigid *rotating* Wigner molecule that exhibits a rigid moment of inertia. Then the states inside the low-energy band (two states for $N=2$, three for $N=3$, six for $N=4$, etc.) do not become degenerate in energy but form an yrast rotational band[49] specified by $L^2/2\mathcal{J}_0$, where L is the total angular momentum and $\mathcal{J}_0$ is the classical moment of inertia. We note that the energy splittings among the yrast rotational states are much smaller than the vibrational energy gap in circular dots associated with the quantum of energy $\sqrt{3}\hbar\omega_0$ of the stretching (often referred to as breathing) mode of the polygonal-ring configuration of the quasiclassical Wigner molecule.[50–52]

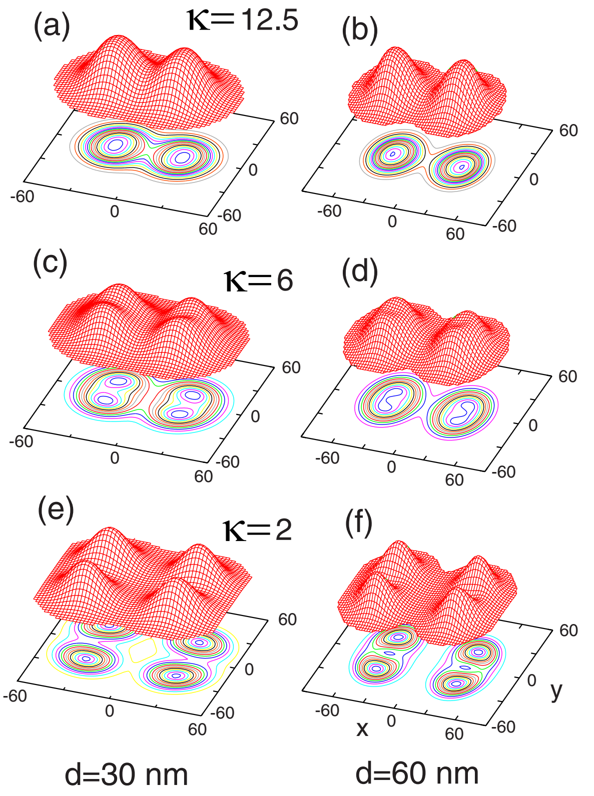

FIG. 5. (Color online) Electron densities at $B=0$ for the ground state (with $S=0$, $S_z=0$, parity $P_{xy}=1$) for $N=4$ electrons in a double quantum dot with interdot separations $d=30$ nm (left column) and $d=60$ nm (right column). The top (a,b), middle (c,d), and bottom (e,f) rows correspond to $\kappa=12.5$ (weak repulsion), $\kappa=6$ (intermediate repulsion), and $\kappa=2$ (strong repulsion), respectively. Ground-state energies: (a) $E=27.609$ meV, (b) $E=21.572$ meV, (c) $E=49.217$ meV, (d) $E=39.799$ meV, (e) $E=111.361$ meV, and (f) $E=94.516$ meV (compare Figs. 3 and 4). The interdot barrier corresponds to $\epsilon^b=0.5$. Distances in nm. Vertical axis in arbitrary units (with the same scale for all six panels).

B. Electron densities

The electron density is the expectation value of the one-body operator

$$\hat{\rho}(\mathbf{r})=\sum_{i=1}^{N}\delta(\mathbf{r}-\mathbf{r}_i), \tag{18}$$

that is,

$$\rho(\mathbf{r})=\langle\Phi^{\mathrm{EXD}}_{N,q}|\hat{\rho}(\mathbf{r})|\Phi^{\mathrm{EXD}}_{N,q}\rangle=\sum_{I,J}C^{q*}_{I}C^{q}_{J}\langle\Psi^{N}_{I}|\hat{\rho}(\mathbf{r})|\Psi^{N}_{J}\rangle. \tag{19}$$

Since $\hat{\rho}(\mathbf{r})$ is a one-body operator, it connects only Slater determinants Ψ^N_I and Ψ^N_J that differ at most by *one* spin-orbital $\chi_j(\mathbf{r})$; for the corresponding Slater rules for calculating matrix elements between determinants for one-body operators in terms of spin-orbitals, see Table 2.3 in Ref. 46.

In Figs. 5(a)–5(f), we display (for the aforementioned three strengths of interelectron repulsion) the ground-state electron densities for $N=4$ electrons in the case of a double dot at zero magnetic field with interdot separations $d=30$ nm (left column) and $d=60$ nm (right column).

For the weak interaction case ($\kappa=12.5$) at $B=0$, the electron densities do not exhibit clear signatures of formation of a Wigner molecule for either interdot distance, $d=30$ nm [Fig. 5(a)] or $d=60$ nm [Fig. 5(b)]. The Wigner molecule is well formed, however, in the case of the intermediate Coulomb repulsion [$\kappa=6$; see Figs. 5(c) and 5(d)]. One observes indeed four humps that correspond to the four localized electrons; they are located at (± 34.88 nm, ± 13.13 nm) in the $d=60$ nm case. In the case of strong Coulomb repulsion ($\kappa=2$) and for the same interdot distance $d=60$ nm, the electrons are further localized as can be seen from Fig. 5(f); the four humps occur now at (± 39.86 nm, ± 21.02 nm). The Wigner molecule is also well formed in the strong-repulsion and $d=30$ nm case, as can be seen from Fig. 5(e), with the localized electrons located at (± 29.28 nm, ± 21.11 nm).

C. Spin-resolved conditional probability distributions

1. Definitions

In the regime corresponding to a well-defined Wigner molecule, the electron densities (see Sec. V B) are characterized by four humps that reflect the localization of the four electrons in the double quantum dot. Such charge densities do not provide any information concerning the spin structure of each EXD state. In fact, all six EXD states in the lower band exhibit very similar four-humped electron densities.

The spin configurations associated with a given (S,S_z) EXD state in the WM regime can be explored with the help of the spin-resolved two-point anisotropic correlation function defined as:

$$P_{\sigma\sigma_0}(\mathbf{r},\mathbf{r}_0)=\langle\Phi^{\mathrm{EXD}}_{N,q}|\sum_{i\neq j}\delta(\mathbf{r}-\mathbf{r}_i)\delta(\mathbf{r}_0-\mathbf{r}_j)\delta_{\sigma\sigma_i}\delta_{\sigma_0\sigma_j}|\Phi^{\mathrm{EXD}}_{N,q}\rangle, \tag{20}$$

with the EXD many-body wave function given by equation (7).

Using a normalization constant

$$\mathcal{N}(\sigma,\sigma_0,\mathbf{r}_0)=\int P_{\sigma\sigma_0}(\mathbf{r},\mathbf{r}_0)d\mathbf{r}, \tag{21}$$

we further define a related conditional probability distribution (CPD) as

$$\mathcal{P}_{\sigma\sigma_0}(\mathbf{r},\mathbf{r}_0)=P_{\sigma\sigma_0}(\mathbf{r},\mathbf{r}_0)/\mathcal{N}(\sigma,\sigma_0,\mathbf{r}_0), \tag{22}$$

having the property $\int\mathcal{P}_{\sigma\sigma_0}(\mathbf{r},\mathbf{r}_0)d\mathbf{r}=1$. The spin-resolved CPD gives the spatial probability distribution of finding a second electron with spin projection σ under the condition that another electron is located (fixed) at $\mathbf{r}_0$ with spin projection σ_0; σ and σ_0 can be either up (↑) or down (↓).

To calculate $P_{\sigma\sigma_0}(\mathbf{r},\mathbf{r}_0)$ in Eq. (20), we use a symmetrized operator

$$\hat{T}_{\sigma\sigma_0}(\mathbf{r},\mathbf{r}_0) = \sum_{i<j} [\delta(\mathbf{r}-\mathbf{r}_i)\delta(\mathbf{r}_0-\mathbf{r}_j)\delta_{\sigma\sigma_i}\delta_{\sigma_0\sigma_j} + \delta(\mathbf{r}-\mathbf{r}_j)\delta(\mathbf{r}_0-\mathbf{r}_i)\delta_{\sigma\sigma_j}\delta_{\sigma_0\sigma_i}], \quad (23)$$

yielding

$$P_{\sigma\sigma_0}(\mathbf{r},\mathbf{r}_0) = \langle \Phi^{\mathrm{EXD}}_{N,q} | \hat{T} | \Phi^{\mathrm{EXD}}_{N,q} \rangle = \sum_{I,J} C_I^{q*} C_J^{q} \langle \Psi_I^N | \hat{T} | \Psi_J^N \rangle. \quad (24)$$

Since $\hat{T}_{\sigma\sigma_0}(\mathbf{r},\mathbf{r}_0)$ is a two-body operator, it connects only Slater determinants Ψ_I^N and Ψ_J^N that differ at most by *two* spin-orbitals $\chi_{j_1}(\mathbf{r})$ and $\chi_{j_2}(\mathbf{r})$; for the corresponding Slater rules for calculating matrix elements between determinants for two-body operators in terms of spin-orbitals, see Table 2.4 in Ref. 46.

2. Examples of $S=0$, $S_z=0$ EXD states at $B=0$

For each charge density corresponding to a given state of the system, one can plot four different spin-resolved CPDs, i.e., $\mathcal{P}_{\uparrow\uparrow}$, $\mathcal{P}_{\uparrow\downarrow}$, $\mathcal{P}_{\downarrow\uparrow}$, and $\mathcal{P}_{\downarrow\downarrow}$. This can potentially lead to a very large number of time-consuming computations and an excessive number of plots. For studying the spin structure of the $S=0$, $S_z=0$ states at $B=0$, however, we found that knowledge of a single CPD, taken here to be $\mathcal{P}_{\uparrow\downarrow}$ (see Fig. 6), is sufficient in the regime of Wigner-molecule formation. Indeed, the specific angle θ specifying the spin function $\mathcal{X}_{00}$ Eq. (15) corresponding to the CPDs portrayed in Fig. 6 can be determined through the procedure described in the following:

We designate with roman indices I, II, III, and IV the four quadrants of the (x,y) plane, starting with the upper left quadrant and going clockwise [see Fig. 6(a)]. In the case of a 4*e* Wigner molecule, a single electron is localized within each quadrant. The same roman indices designate also the positions of the localized electrons in each of the six Slater determinants (e.g., $|\uparrow\uparrow\downarrow\downarrow\rangle$, $|\uparrow\downarrow\uparrow\downarrow\rangle$, etc.) that enter into the spin function $\mathcal{X}_{00}$ in Eq. (15). We take always the fixed point to correspond to the fourth (IV) quadrant [bottom left in Fig. 6(a)]. An inspection of Eq. (15) shows that only three Slater determinants in $\mathcal{X}_{00}$ contribute to $\mathcal{P}_{\uparrow\downarrow}$, namely, $|\uparrow\uparrow\downarrow\downarrow\rangle$, $|\uparrow\downarrow\uparrow\downarrow\rangle$, and $|\downarrow\uparrow\uparrow\downarrow\rangle$; these are the only determinants in Eq. (15) with a down spin in the fourth quadrant. From these three Slater determinants, only the first and the second contribute to the conditional probability $\Pi_{\uparrow\downarrow}(\mathrm{I})$ of finding another electron with spin-up in quadrant I; this corresponds to the volume under the hump of the EXD CPD in quadrant I [see, e.g., the hump in Fig. 6(a)]. Taking the squares of the coefficients of $|\uparrow\uparrow\downarrow\downarrow\rangle$ and $|\uparrow\downarrow\uparrow\downarrow\rangle$ in Eq. (15), one gets

$$\Pi_{\uparrow\downarrow}(\mathrm{I}) \propto \frac{\sin^2\theta}{3} + \left(\frac{1}{2}\cos\theta - \sqrt{\frac{1}{12}}\sin\theta\right)^2. \quad (25)$$

Similarly, one finds that only $|\uparrow\uparrow\downarrow\downarrow\rangle$ and $|\downarrow\uparrow\uparrow\downarrow\rangle$ contribute to $\Pi_{\uparrow\downarrow}(\mathrm{II})$ and that

$$\Pi_{\uparrow\downarrow}(\mathrm{II}) \propto \frac{\sin^2\theta}{3} + \left(\frac{1}{2}\cos\theta + \sqrt{\frac{1}{12}}\sin\theta\right)^2. \quad (26)$$

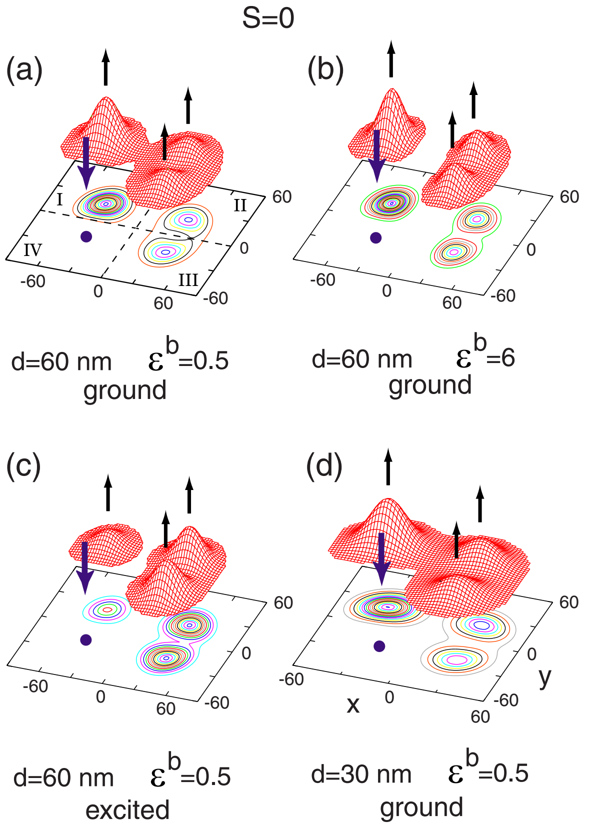

FIG. 6. (Color online) CPDs $\mathcal{P}_{\uparrow\downarrow}$ at $B=0$ for several EXD states with $S=0$, $S_z=0$, and parity $P_{xy}=1$ of $N=4$ electrons in a double quantum dot with interdot separations $d=60$ nm (a-c) and $d=30$ nm (d). Case of strong Coulomb repulsion ($\kappa=2$) with an interdot barrier $\epsilon^b=0.5$ (a,c-d) and $\epsilon^b=6$ (b). Panels (a-b,d) correspond to ground states. Panel (c) corresponds to the excited second $S=0$ state for the same parameters as in panel (a) [see Fig. 4(c) and the branching diagram in Fig. 2]. Energies: (a) $E=94.516$ meV, (b) $E=96.811$ meV, (c) $E=95.017$ meV, and (d) $E=111.361$ meV [compare Figs. 3(c) and 4(c)]. Distances in nm. Vertical axis in arbitrary units (with the same scale for all panels in Figs. 6–8). The fixed point is located at the maximum of the hump in the lower-left quadrant of the corresponding electron density, i.e., at $\mathbf{r}_0=(-40\text{ nm},-21\text{ nm})$ for panels (a-c) and $\mathbf{r}_0=(-29\text{ nm},-19\text{ nm})$ for panel (d).

Integrating under the humps of the EXD CPD in quadrants I and II, we determine numerically the ratio $\Pi_{\uparrow\downarrow}(\mathrm{I})/\Pi_{\uparrow\downarrow}(\mathrm{II})$, which allows us to specify the absolute value of θ (within the interval $-90° \leq \theta \leq 90°$) via the expressions in Eqs. (25) and (26). The restriction to the absolute value of θ is a result of the squares of the sine and cosine entering in $\Pi_{\uparrow\downarrow}(\mathrm{I})$ and $\Pi_{\uparrow\downarrow}(\mathrm{II})$. To obtain the actual sign of θ, additional information is needed: for example the ratio $\Pi_{\uparrow\downarrow}(\mathrm{I})/\Pi_{\uparrow\downarrow}(\mathrm{III})$ can be used in a similar way, where

$$\Pi_{\uparrow\downarrow}(\mathrm{III}) \propto \left(\frac{1}{2}\cos\theta - \sqrt{\frac{1}{12}}\sin\theta\right)^2 + \left(\frac{1}{2}\cos\theta + \sqrt{\frac{1}{12}}\sin\theta\right)^2. \quad (27)$$

Using the method described above, we find that $\theta \approx -60°$ for the EXD ground state at $d=60$ nm (larger interdot distance) and $\kappa=2$ [strong repulsion; see Fig. 6(a)], and the corresponding spin function simplifies to

$$\mathcal{X}_{00}^{(1)} = -\frac{1}{2}|\uparrow\uparrow\downarrow\downarrow\rangle + \frac{1}{2}|\uparrow\downarrow\uparrow\downarrow\rangle + \frac{1}{2}|\downarrow\uparrow\downarrow\uparrow\rangle - \frac{1}{2}|\downarrow\downarrow\uparrow\uparrow\rangle. \quad (28)$$

Remarkably, increasing the interdot barrier from $\epsilon^b=0.5$ [Fig. 6(a)] to $\epsilon^b=6$ [Fig. 6(b)], while keeping the other parameters constant, does not influence much the composition of the associated spin function, which remains that given by Eq. (28). This happens in spite of the visible change in the degree of localization in the electronic orbitals, with the higher interdot-barrier case exhibiting a sharper localization.

In Fig. 6(c), we display the $\mathcal{P}_{\uparrow\downarrow}$ CPD for an excited state with $S=0$, $S_z=0$ (having $P_{xy}=1$ and energy $E=95.017$ meV), with the remaining parameters being the same as in Fig. 6(a). For this case, following an analysis as described above, we found the angle $\theta \approx 30°$, which is associated with a spin function of the form

$$\mathcal{X}_{00}^{(2)} = \frac{1}{2\sqrt{3}}|\uparrow\uparrow\downarrow\downarrow\rangle + \frac{1}{2\sqrt{3}}|\uparrow\downarrow\uparrow\downarrow\rangle - \frac{1}{\sqrt{3}}|\uparrow\downarrow\downarrow\uparrow\rangle - \frac{1}{\sqrt{3}}|\downarrow\uparrow\uparrow\downarrow\rangle + \frac{1}{2\sqrt{3}}|\downarrow\uparrow\downarrow\uparrow\rangle + \frac{1}{2\sqrt{3}}|\downarrow\downarrow\uparrow\uparrow\rangle. \quad (29)$$

We note that the spin functions in Eqs. (28) and (29) are orthogonal.

In Fig. 6(d), we display the $\mathcal{P}_{\uparrow\downarrow}$ CPD for the ground state with $S=0$, $S_z=0$ (having $P_{xy}=1$ and energy $E=111.361$ meV) and for the shorter interdot distance $d=30$ nm. For this case, we found an angle $\theta \approx -63.08°$, which corresponds to the following spin function:

$$\mathcal{X}_{00}^{(3)} = -0.5148|\uparrow\uparrow\downarrow\downarrow\rangle + 0.4838|\uparrow\downarrow\uparrow\downarrow\rangle + 0.031|\uparrow\downarrow\downarrow\uparrow\rangle + 0.031|\downarrow\uparrow\uparrow\downarrow\rangle + 0.4838|\downarrow\uparrow\downarrow\uparrow\rangle - 0.5148|\downarrow\downarrow\uparrow\uparrow\rangle. \quad (30)$$

From a comparison of the above result with that for the larger $d=60$ nm [see Eq. (28)], we conclude that the difference in interdot distance results in a slight variation in the spin functions.

3. Examples of $S=1$, $S_z=0$ EXD states at $B=0$

In this section, we turn our attention to partially polarized EXD states with $S=1$. In Fig. 7(a), we display the $\mathcal{P}_{\uparrow\downarrow}$ CPD at $B=0$ for an excited state with $S=1$, $S_z=0$, parity $P_{xy}=1$, and energy $E=94.757$ meV, at the larger interdot separation $d=60$ nm. Again we consider the case of strong Coulomb repulsion ($\kappa=2$) with an interdot barrier $\epsilon^b=0.5$. The corresponding spin function $\mathcal{X}_{10}$ [Eq. (16)] depends on two different angles θ and ϕ and one needs at least two different CPDs for determining their specific values. For this purpose, we display also the $\mathcal{P}_{\downarrow\downarrow}$ CPD for the same state in Fig. 7(b).

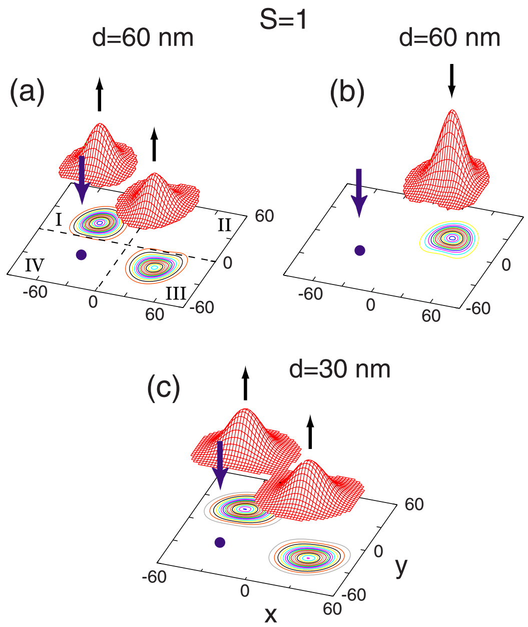

FIG. 7. (Color online) CPDs at $B=0$ for excited EXD states with $S=1$, $S_z=0$, and parity $P_{xy}=1$ of $N=4$ electrons in a double quantum dot at the larger interdot separation $d=60$ nm (a-b) and the shorter interdot separation $d=30$ nm (c). Panels (a) and (c) display $\mathcal{P}_{\uparrow\downarrow}$ CPDS (down-up), while panel (b) displays a different $\mathcal{P}_{\downarrow\downarrow}$ CPD (down-down), but for the *same* state as in (a). Case of strong Coulomb repulsion ($\kappa=2$) with interdot barrier $\epsilon^b=0.5$. Energies: (a-b) $E=94.757$ meV, and (c) $E=111.438$ meV [compare Figs. 3(c) and 4(c)]. Distances in nm. Vertical axis in arbitrary units (with the same scale for all panels in Figs. 6–8). The fixed point is located at the maximum of the hump in the lower-left quadrant of the corresponding electron density, i.e., at $\mathbf{r}_0=(-40\text{ nm},-21\text{ nm})$ for panels (a-b) and $\mathbf{r}_0=(-29\text{ nm},-19\text{ nm})$ for panel (c). Note that this is a case with $S=1$; the previous Fig. 6 displayed $S=0$ cases.

The specific values of θ and ϕ associated with the CPDs in Figs. 7(a) and 7(b) can be determined through the ratios $\Pi_{\uparrow\downarrow}(\mathrm{I})/\Pi_{\uparrow\downarrow}(\mathrm{II})$ and $\Pi_{\uparrow\downarrow}(\mathrm{I})/\Pi_{\uparrow\downarrow}(\mathrm{III})$ [associated with Fig. 7(a)] and $\Pi_{\downarrow\downarrow}(\mathrm{I})/\Pi_{\downarrow\downarrow}(\mathrm{II})$ and $\Pi_{\downarrow\downarrow}(\mathrm{I})/\Pi_{\downarrow\downarrow}(\mathrm{III})$ [associated with Fig. 7(b)], where

$$\Pi_{\uparrow\downarrow}(\mathrm{I}) \propto \frac{1}{3}\sin^2\theta\sin^2\phi + \frac{5}{12}\sin^2\theta\cos^2\phi + \frac{1}{4}\cos^2\theta + \frac{\sqrt{2}}{6}\sin^2\theta\sin\phi\cos\phi + \frac{1}{\sqrt{6}}\sin\theta\cos\theta\sin\phi - \frac{1}{\sqrt{12}}\sin\theta\cos\theta\cos\phi, \quad (31)$$

$$\Pi_{\uparrow\downarrow}(\mathrm{II}) \propto \frac{1}{3}\sin^2\theta\sin^2\phi + \frac{5}{12}\sin^2\theta\cos^2\phi + \frac{1}{4}\cos^2\theta + \frac{\sqrt{2}}{6}\sin^2\theta\sin\phi\cos\phi - \frac{1}{\sqrt{6}}\sin\theta\cos\theta\sin\phi + \frac{1}{\sqrt{12}}\sin\theta\cos\theta\cos\phi, \quad (32)$$

$$\Pi_{\uparrow\downarrow}(\text{III}) \propto \frac{1}{3}\sin^2\theta\sin^2\phi + \frac{1}{6}\sin^2\theta\cos^2\phi - \frac{\sqrt{2}}{3}\sin^2\theta\sin\phi\cos\phi + \frac{1}{2}\cos^2\theta, \tag{33}$$

and

$$\Pi_{\downarrow\downarrow}(\text{I}) \propto \left(\sqrt{\frac{1}{6}}\sin\theta\sin\phi - \sqrt{\frac{1}{12}}\sin\theta\cos\phi - \frac{1}{2}\cos\theta\right)^2, \tag{34}$$

$$\Pi_{\downarrow\downarrow}(\text{II}) \propto \left(\sqrt{\frac{1}{6}}\sin\theta\sin\phi - \sqrt{\frac{1}{12}}\sin\theta\cos\phi + \frac{1}{2}\cos\theta\right)^2, \tag{35}$$

$$\Pi_{\downarrow\downarrow}(\text{III}) \propto \left(\sqrt{\frac{1}{6}}\sin\theta\sin\phi + \sqrt{\frac{1}{3}}\sin\theta\cos\phi\right)^2. \tag{36}$$

Using Eqs. (31)–(36) and the numerical values of the ratios $\Pi_{\uparrow\downarrow}(\text{I})/\Pi_{\uparrow\downarrow}(\text{II})$ and $\Pi_{\uparrow\downarrow}(\text{I})/\Pi_{\uparrow\downarrow}(\text{III})$ $\Pi_{\downarrow\downarrow}(\text{I})/\Pi_{\downarrow\downarrow}(\text{II})$ and $\Pi_{\downarrow\downarrow}(\text{I})/\Pi_{\downarrow\downarrow}(\text{III})$ (specified via a volume integration under the humps of the EXD CPDs), we determined that $\theta=-45°$ and $\sin\phi=-\sqrt{2/3}$, $\cos\phi=\sqrt{1/3}$ (i.e., $\phi\approx-54.736°$). Thus, the corresponding spin function reduces to the simple form

$$\mathcal{X}_{10} = \sqrt{\frac{1}{2}}|\uparrow\downarrow\uparrow\downarrow\rangle - \sqrt{\frac{1}{2}}|\downarrow\uparrow\downarrow\uparrow\rangle. \tag{37}$$

In Fig. 7(c), we display the $\mathcal{P}_{\uparrow\downarrow}$ CPD at $B=0$ for a similar excited state as in Fig. 7(a) (with $S=1$, $S_z=0$, parity $P_{xy}=1$, and energy $E=111.438$ meV) of $N=4$ electrons at the shorter interdot separation $d=30$ nm. Here too we consider the case of strong Coulomb repulsion ($\kappa=2$) with interdot barrier $\epsilon^b=0.5$. We note that the localization of electrons is stronger for the larger interdot distance [compare Fig. 7(a) with Fig. 7(c)]. This difference, however, does not influence the coefficients entering into the associated spin function, which we found to remain very close to the specific form in Eq. (37).

4. *Spin-resolved conditional probability distributions at $B\neq 0$*

In Fig. 8 we display EXD CPDs at a finite value of the magnetic field, and precisely at $B=2$ T, for the two states of the low-energy band with $S=0$, $S_z=0$ (at the larger interdot separation $d=60$ nm and strong interelectron repulsion $\kappa=2$). This value of B was chosen to lie beyond the crossing point for the six states of the low-energy band [which happens at $B\sim 1$ T; see Fig. 4(c)]. Comparison with the CPDs of the corresponding states at zero magnetic field [see Figs. 6(a) and 6(c)] shows that the spin structure of the associated Wigner molecule varies rather slowly with the increasing magnetic field in the range $0\leq B\leq 2.5$ T.

Following the height of the humps in the left upper quadrants, one observes that the CPD in Fig. 8(a) (case of *lower-energy* state at $B=2$ T with $S=0$ and $P_{xy}=1$) corresponds to that of Fig. 6(a) (case of lower-energy state at $B=0$ with $S=0$ and $P_{xy}=1$). Similarly, the CPD in Fig. 8(b) at $B=2$ T (*higher-energy* state) corresponds to that of Fig. 6(c) at $B=0$ (higher-energy state). From these results, we concludes that the two states with $S=0$ and $P_{xy}=1$ do not really cross at the "crossing" point at $B\sim 1$ T. In reality, this point is an anticrossing point for these two states, although the anticrossing gap is too small to be seen with the naked eye. This behavior agrees with that expected from states having the same quantum numbers. We checked that a similar observation applies for the two other states in the low-energy band having the same quantum numbers, i.e., those having $S=1$ and $P_{xy}=-1$.

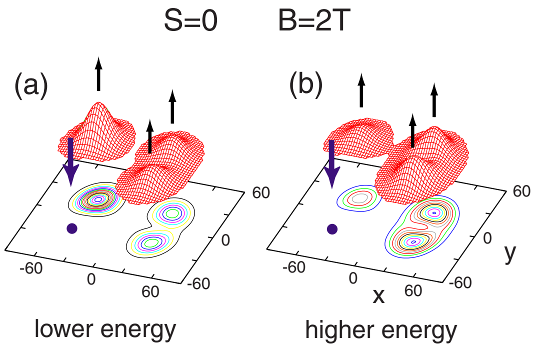

lower energy higher energy

FIG. 8. (Color online) $\mathcal{P}_{\uparrow\downarrow}$ CPDs for the EXD states at $B=2$ T with $S=0$, $S_z=0$, and parity $P_{xy}=1$ of $N=4$ electrons in a double quantum dot at the larger interdot separation $d=60$ nm. (a) The lower energy of the two $S=0$ states (see branching diagram in Fig. 2). (b) Higher energy $S=0$ state. Case of strong Coulomb repulsion ($\kappa=2$) with interdot barrier $\epsilon^b=0.5$. Energies: (a) $E=94.605$ meV and (b) $E=95.047$ meV [compare Fig. 4(c)]. Distances in nm. Vertical axis in arbitrary units (with the same scale for all panels in Figs. 6–8). The fixed point is located at $\mathbf{r}_0=(-40\text{ nm},-21\text{ nm})$.

VI. ANALOGIES WITH A FOUR-SITE HEISENBERG SPIN CLUSTER

In Sec. V C, using the spin-resolved CPDs, we showed that the EXD many-body wave functions in the Wigner-molecule regime can be expressed as a linear superposition of a small number of Slater determinants and that this superposition exhibits the structure expected from the theory of many-body spin functions. This finding naturally suggests a strong analogy with the field of nanomagnets and quantum magnetism, usually studied via the explicitly spin-dependent model effective Hamiltonian known as the Heisenberg Hamiltonian,[14,15,53] given by $\mathcal{H}_H'=\Sigma_{i,j}J_{ij}\mathbf{S}_i\cdot\mathbf{S}_j$, where J_{ij} are the exchange integrals between spins on sites i and j. Even in its more familiar, simpler form

$$\mathcal{H}_H = \sum_{\langle i,j\rangle} J_{ij}\mathbf{S}_i\cdot\mathbf{S}_j, \tag{38}$$

that is that of the spin-1/2 Heisenberg antiferromagnet with nearest-neighbor interactions only and $J_{ij}>0$, it is well known that the zero-temperature (at $B=0$) solutions of Hamiltonian (38) involve radically different forms as a function of the geometry, dimensionality, and size.

Generalizing this behavior to finite magnetic fields B, we have found that the rich variety of the EXD energy spectra presented in Figs. 3 and 4, as well as the EXD spin functions of Sec. V C, can be related to those of a four-site Heisenberg Hamiltonian $\mathcal{H}_H^{\mathrm{RP}}(B)$ with B-dependent exchange constants $\tilde{J}_{ij}(B)=J_{ij}F_{ij}(B)$, and with the four electrons being located at the vertices of a rectangular parallelogram (RP) as discussed earlier. Due to the reflection symmetry, $\mathcal{H}_H^{\mathrm{RP}}(B)$ has only two different exchange constants $\tilde{J}_{12}=\tilde{J}_{34}$ and $\tilde{J}_{14}=\tilde{J}_{23}$, i.e.,

$$\mathcal{H}_H^{\mathrm{RP}}(B)=\tilde{J}_{12}(B)(\mathbf{S}_1\cdot\mathbf{S}_2+\mathbf{S}_3\cdot\mathbf{S}_4)+\tilde{J}_{14}(B)(\mathbf{S}_1\cdot\mathbf{S}_4+\mathbf{S}_2\cdot\mathbf{S}_3), \tag{39}$$

where $1\rightarrow\mathrm{I}$, $2\rightarrow\mathrm{II}$, $3\rightarrow\mathrm{III}$, and $4\rightarrow\mathrm{IV}$ [in a clockwise direction, see Fig. 6(a)]. Since the $B=0$ spin exchange interaction constants J_{ij} are expected to decrease exponentially[54] with the distance between the two sites i and j, one expects that the Heisenberg model will reproduce the present EXD results in the regime $J_{12}\ll J_{14}$.

To proceed, it is sufficient to use the six-dimensional Ising Hilbert subspace for zero total-spin projection ($S_z=0$), which is spanned by the following set of basis states [we follow here the ordering in Eq. (15)]: $|1\rangle\rightarrow|\uparrow\uparrow\downarrow\downarrow\rangle$, $|2\rangle\rightarrow|\uparrow\downarrow\uparrow\downarrow\rangle$, $|3\rangle\rightarrow|\uparrow\downarrow\downarrow\uparrow\rangle$, $|4\rangle\rightarrow|\downarrow\uparrow\uparrow\downarrow\rangle$, $|5\rangle\rightarrow|\downarrow\uparrow\downarrow\uparrow\rangle$, and $|6\rangle\rightarrow|\downarrow\downarrow\uparrow\uparrow\rangle$. In this subspace, the Heisenberg Hamiltonian given by Eq. (39) can be written in matrix form as

$$\mathcal{H}_H^{\mathrm{RP}}(B)=\frac{1}{2}\begin{pmatrix} \tilde{J}_{12}-\tilde{J}_{14} & \tilde{J}_{14} & 0 & 0 & \tilde{J}_{14} & 0 \\ \tilde{J}_{14} & -(\tilde{J}_{12}+\tilde{J}_{14}) & \tilde{J}_{12} & \tilde{J}_{12} & 0 & \tilde{J}_{14} \\ 0 & \tilde{J}_{12} & \tilde{J}_{14}-\tilde{J}_{12} & 0 & \tilde{J}_{12} & 0 \\ 0 & \tilde{J}_{12} & 0 & \tilde{J}_{14}-\tilde{J}_{12} & \tilde{J}_{12} & 0 \\ \tilde{J}_{14} & 0 & \tilde{J}_{12} & \tilde{J}_{12} & -(\tilde{J}_{12}+\tilde{J}_{14}) & \tilde{J}_{14} \\ 0 & \tilde{J}_{14} & 0 & 0 & \tilde{J}_{14} & \tilde{J}_{12}-\tilde{J}_{14} \end{pmatrix}. \tag{40}$$

A lengthy, but straightforward, calculation yields the general eigenvalues $\mathcal{E}_i$ and corresponding eigenvectors $\mathcal{V}_i$ of matrix (40). The eigenvalues are

$$\mathcal{E}_1=-(\tilde{J}_{14}+\tilde{J}_{12})/2, \tag{41}$$

$$\mathcal{E}_2=(\tilde{J}_{14}-\tilde{J}_{12})/2, \tag{42}$$

$$\mathcal{E}_3=(\tilde{J}_{12}-\tilde{J}_{14})/2, \tag{43}$$

$$\mathcal{E}_4=(\tilde{J}_{14}+\tilde{J}_{12})/2, \tag{44}$$

$$\mathcal{E}_5=-(\tilde{J}_{14}+\tilde{J}_{12})/2-Q(\tilde{J}_{14},\tilde{J}_{12}), \tag{45}$$

$$\mathcal{E}_6=-(\tilde{J}_{14}+\tilde{J}_{12})/2+Q(\tilde{J}_{14},\tilde{J}_{12}), \tag{46}$$

where

$$Q(a,b)=\sqrt{a^2-ab+b^2}. \tag{47}$$

The corresponding unnormalized eigenvectors and their total spins are given by

$$\mathcal{V}_1=\{0,-1,0,0,1,0\}, \quad S=1, \tag{48}$$

$$\mathcal{V}_2=\{0,0,-1,1,0,0\}, \quad S=1, \tag{49}$$

$$\mathcal{V}_3=\{-1,0,0,0,0,1\}, \quad S=1, \tag{50}$$

$$\mathcal{V}_4=\{1,1,1,1,1,1\}, \quad S=2, \tag{51}$$

$$\mathcal{V}_5=\{1,-\mathcal{X},-1+\mathcal{X},-1+\mathcal{X},-\mathcal{X},1\}, \quad S=0, \tag{52}$$

$$\mathcal{V}_6=\{1,-\mathcal{Y},-1+\mathcal{Y},-1+\mathcal{Y},-\mathcal{Y},1\}, \quad S=0, \tag{53}$$

where

$$\mathcal{X}=r+Q(1,r), \tag{54}$$

$$\mathcal{Y}=r-Q(1,r), \tag{55}$$

and $r=\tilde{J}_{12}/\tilde{J}_{14}$.

To understand how the Heisenberg Hamiltonian in Eq. (39) captures the rich behavior seen in the EXD spectra of Figs. 3 and 4, we start with the limiting case $r\rightarrow 0$, which is applicable (see below) to the larger interdot distance $d=60$ nm. In this limit, one can neglect $\tilde{J}_{12}$ compared with $\tilde{J}_{14}$, which results in partial degeneracies within the band; namely one has $\mathcal{E}_2=\mathcal{E}_4=\mathcal{E}_6=\tilde{J}_{14}/2$, $\mathcal{E}_1=\mathcal{E}_3=-\tilde{J}_{14}/2$, and $\mathcal{E}_5=-3\tilde{J}_{14}/2$. This 3-2-1 degeneracy pattern is independent of the magnetic-field dependence through $F_{14}(B)$ [$\tilde{J}_{ij}=J_{ij}F_{ij}(B)$] and is characteristic of all three EXD spectra (for $\kappa=12.5$, 6, and 2) associated with the larger interdot distance $d=60$ nm. Furthermore, the fact that all six curves in the EXD lowest-energy band appear to cross at the same point $B^C(\kappa)$ (reversing at the same time the order of the degenerate levels) suggests that

$$F_{14}(B)\sim\cos[\pi B/(2B_{14}^C)]. \tag{56}$$

It is remarkable that the behavior described above is prominent even for the weak interelectron repulsion $\kappa=12.5$ [see

Fig. 4(a)] when the extent of electron localization and the formation of a Wigner molecule are not clearly visible via an inspection of the corresponding electron densities [see Fig. 5(b)].

Of interest is the fact that the ability of the Heisenberg Hamiltonian in Eq. (39) to reproduce the EXD trends is not restricted solely to energy spectra but extends to the EXD wave functions as well. Indeed when $\tilde{J}_{12} \to 0$, the last two eigenvectors of the Heisenberg matrix (having $S=0$) become

$$\mathcal{V}_5 \to \{1,-1,0,0,-1,1\} \tag{57}$$

and

$$\mathcal{V}_6 \to \{1,1,-2,-2,1,1\}. \tag{58}$$

When multiplied by the normalization factor, the wave functions represented by the eigenvectors in Eqs. (57) and (58) coincide (within an overall ∓ 1 sign) with the EXD spin functions $\mathcal{X}_{00}^{(1)}$ and $\mathcal{X}_{00}^{(2)}$ in Eqs. (28) and (29), respectively. In addition, when again multiplied by the corresponding normalization factor, the wave function represented by the eigenvector $\mathcal{V}_1$ [Eq. (48)] (having total spin $S=1$) coincides (within an overall minus sign) with the EXD spin function $\mathcal{X}_{10}$ in Eq. (37).

The EXD spectra and spin functions for the shorter distance $d=30$ nm can be analyzed within the framework of the four-site Heisenberg Hamiltonian (40) when small (compared with $\tilde{J}_{14}$), but non-negligible, values of the second exchange integral $\tilde{J}_{12}$ are considered. In this case, the partial threefold and twofold degeneracies are lifted. Indeed in Fig. 3(a) ($\kappa=12.5$) and Fig. 3(b) ($\kappa=6$), the EXD lowest-energy band consists of six distinct levels. For the strong interelectron case with $\kappa=2$ and $d=30$ nm [Fig. 3(c)], however, the EXD spectra indicate that the effective (self-consistent field) potential barrier between the dots due to the Coulomb repulsion is high enough to reduce $\tilde{J}_{12}$ to a negligible value and to produce spectra exhibiting the characteristic 3-2-1 degeneracy pattern that is prominent in the spectra associated with the larger interdot distance $d=60$ nm. (For the wave functions in the $\kappa=2$ and $d=30$ nm case, however, the influence of $\tilde{J}_{12}$ cannot be neglected, see below.)

In addition to the lifting of the partial degeneracies within the lowest-energy band, one observes from an examination of Figs. 3(a) and 3(b) the occurrence of two characteristic secondary oscillations (as a function of B) emerging out of the previously threefold and twofold degenerate levels. Using the Heisenberg Hamiltonian, these secondary oscillations can be described by taking the second exchange constant to have a B dependence similar to that in Eq. (56), i.e.,

$$F_{12}(B) \sim \cos[\pi B/(2B_{12}^C) + \phi_0], \tag{59}$$

with $B_{12}^C < B_{14}^C$, ϕ_0 being a phase shift. This secondary oscillation is superimposed on the main oscillation specified by $F_{14}(B)$ [Eq. (56)] in accordance with the expressions for the Heisenberg energy levels $\mathcal{E}_2$ [Eq. (42)], $\mathcal{E}_4$ [Eq. (44)], $\mathcal{E}_6$ [Eq. (46)], $\mathcal{E}_1$ [Eq. (41)], and $\mathcal{E}_3$ [Eq. (43)].

Another characteristic feature developing for $d=30$ nm in Figs. 3(a) and 3(b) is the anticrossing gap Δ between the two $S=0$ states. According to the Heisenberg model this gap is given by $\Delta = 2J_{12}\cos[\pi B_{14}^C/(2B_{12}^C) + \phi_0]$. As a concrete example of the above, we estimated that the spectrum of Fig. 3(b) can be rather well reproduced using the expressions for the Heisenberg eigenvalues when $J_{12}/J_{14} \approx -1/4.1$, $B_{12}^C \approx B_{14}^C/2.5$, and $\phi_0 = \pi/2.4$.

Similar to the findings in the larger-distance ($d=60$ nm) case, the agreement between EXD and Heisenberg-model results in the smaller $d=30$ nm distance includes also the wave functions. Indeed, as discussed in Sec. III, the $P_{xy}=1$, $S=1$ EXD spin function for $d=30$ nm (and $B=0$, $\kappa=2$) was found to be identical to the one determined for the larger interdot distance $d=60$ nm, i.e., it is given by expression (37). This reflects the remarkable property that the Heisenberg eigenvector $\mathcal{V}_1$ [Eq. (48)] is independent of the two exchange constants $\tilde{J}_{14}$ and $\tilde{J}_{12}$ and thus independent of the interdot distance d (as well as of the dielectric constant κ and the magnetic field B). On the other hand, the $S=0$ Heisenberg eigenvectors [Eqs. (52) and (53)] do depend on the ratio $r = \tilde{J}_{12}/\tilde{J}_{14}$, which is in agreement with the fact that the EXD ground-state spin function $\mathcal{X}_{00}^{(3)}$ for $d=30$ nm in Eq. (30) is slightly different from the corresponding $S=0$ EXD spin function $\mathcal{X}_{00}^{(1)}$ for $d=60$ nm [see Eq. (28)]. With consideration of the normalization factor, we estimate that the Heisenberg eigenvector $\mathcal{V}_5$ [Eq. (52)] agrees with $\mathcal{X}_{00}^{(3)}$ when $r \approx -1/7.5$.

It is of interest to contrast the EXD spin functions determined in Sec. V C with the well-known solutions of the Heisenberg Hamiltonian [Eq. (39)] when the four spins are located on four sites arranged in a perfect square,[15,16] i.e., when the two exchange integrals are equal; $\tilde{J}_{14} = \tilde{J}_{12} = J > 0$. (The perfect-square arrangement arises[55] also in the case of formation of a four-electron Wigner molecule in a single circular quantum dot.) In this case, the ground state of $\mathcal{H}_H$ is the celebrated resonating valence bond (RVB) state[15,16] which forms the basic unit block in many theoretical approaches aiming at describing high-temperature superconductors.[56] The RVB state has quantum numbers $S=0$ and $S_z=0$ and a Heisenberg energy $\mathcal{E}_5 = -2J$; it is given by the normalized version of $\mathcal{V}_5$ [Eq. (52)] when $r=1$, that is, by (see also Refs. 15 and 16)

$$\mathcal{X}_{00}^{\mathrm{RVB}} = \frac{1}{2\sqrt{3}}|\uparrow\uparrow\downarrow\downarrow\rangle - \frac{1}{\sqrt{3}}|\uparrow\downarrow\uparrow\downarrow\rangle + \frac{1}{2\sqrt{3}}|\uparrow\downarrow\downarrow\uparrow\rangle + \frac{1}{2\sqrt{3}}|\downarrow\uparrow\uparrow\downarrow\rangle - \frac{1}{\sqrt{3}}|\downarrow\uparrow\downarrow\uparrow\rangle + \frac{1}{2\sqrt{3}}|\downarrow\downarrow\uparrow\uparrow\rangle. \tag{60}$$

Although the (excited-state) EXD $\mathcal{X}_{00}^{(2)}$ [Eq. (29)] in the quantum-double-dot case portrayed in Fig. 6(c) appears (superficially) to be similar to the (ground-state) RVB $\mathcal{X}_{00}^{\mathrm{RVB}}$ [Eq. (60)], the two are not equal. Indeed the coefficients of the pair of Slater determinants $|\uparrow\downarrow\uparrow\downarrow\rangle$ and $|\downarrow\uparrow\downarrow\uparrow\rangle$ have been interchanged with those of $|\downarrow\uparrow\uparrow\downarrow\rangle$ and $|\uparrow\downarrow\downarrow\uparrow\rangle$. Similar observations apply also to the remaining pair of $S=0$ and $S_z=0$ states that are orthogonal to $\mathcal{X}_{00}^{(2)}$ [see $\mathcal{X}_{00}^{(1)}$ in Eq. (28);

case of double quantum dot] and to $\mathcal{X}_{00}^{\text{RVB}}$ (case of a perfect square), respectively.

We note that the differences in the $\mathcal{X}_{00}$ spin functions between the DQD case (corresponding to a rectangular parallelogram) and the perfect-square case are also reflected in the $\mathcal{P}_{\uparrow\downarrow}$ CPDs. Indeed the CPDs of the DQD (Fig. 6) exhibit equal-height humps along the smaller side of the parallelogram, while those of the perfect-square configuration (and/or circular quantum dot) exhibit equal-height humps along a diagonal.[55]

VII. DISCUSSION

A. Magnetic-field dependence and relevance to quantum computing

Strongly correlated electrons on a lattice are frequently described by the Hubbard-model Hamiltonian

$$H^{\text{Hubbard}} = -\sum_{i,j,\sigma} t_{ij} c_{i\sigma}^{\dagger} c_{j\sigma} + U \sum_{i} n_{i\uparrow} n_{i\downarrow}, \tag{61}$$

where t_{ij} is the hopping integral from site j to site i, $\sigma = \pm 1$ [equivalently this denotes a spin up ($\uparrow$) or a spin down ($\downarrow$)], and $n_{i\sigma} = c_{i\sigma}^{\dagger} c_{i\sigma}$, with $c_{i\sigma}^{\dagger}$ and $c_{i\sigma}$ being single-particle creation and annihilation operators for the site i. U is the on-site Coulomb repulsion.

It is well known that the one-band Hubbard model at half-filling reduces[57,58] (to lowest order) to a Heisenberg antiferromagnetic Hamiltonian $\mathcal{H}_H$ [see Eq. (38)] in the limit of the on-site Coulomb repulsion $U > 0$ being large relative to the hopping integral t_{ij}. In the absence of an applied magnetic field ($B=0$), t_{ij} can be taken to be real and the corresponding exchange integrals are given by[57]

$$J_{ij}^{\text{Hubbard}} = 2t_{ij}^2 / U. \tag{62}$$

In the presence of a magnetic field (which is the case of this paper), t_{ij} picks up[59,60] a Peierls phase $\exp[(ie/c\hbar)\int_i^j \mathbf{A} \cdot d\mathbf{r}]$, where $\mathbf{A}$ is the vector potential. In this case t_{ij} is complex and one must replace[59,60] $t_{ij}^2 \to t_{ij} t_{ij}^{*}$ in Eq. (62). The complex conjugation, however, cancels any magnetic-field effect associated with the Peierls phase factor, which means that the J_{ij}^{Hubbard} are independent of B.

In sharp contrast with this Hubbard-model result, our EXD calculations indicate that the exchange integrals entering in the Heisenberg Hamiltonian of Eq. (39) depend strongly on the magnetic field. Such strong B dependence of the exchange integrals has been found in previous theoretical studies in the simpler case of two electrons in double quantum dots,[7,21,22,29,30] as well as in anisotropic single quantum dots.[31,32] (For two electrons, the exchange integral is calculated as the energy difference between the singlet and triplet states.) This B dependence in the case of two electrons in quantum dots has also been observed experimentally.[31–33] Following an earlier proposal,[7] the B dependence of J for the two-electron case has developed into a central theme in experimental efforts focusing on solid-state implementation of quantum computing.[2,24] In this context, our EXD results in this paper extend the B dependence of the exchange integrals to larger numbers ($N > 2$) of electrons in quantum-dot molecules.

The physics underlying the emergence of such strong B dependence in the case of solid-state artificial nanostructures is clearly related to the importance[1,5] of orbital magnetic effects resulting from the much larger size (by a factor of 10 000) of the electronic wave functions in 2D quantum dots compared to that in natural atoms. For spin interactions between electrons localized within the natural atoms, huge magnetic fields (of order 10 000 T) are required for reproducing a B dependence of the exchange integrals similar to that discussed in this paper.

B. Aspects of spin entanglement

Néel antiferromagnetic ordering, where the average spin per site $\langle S_j^z \rangle = (-1)^{j+1}/2$, is an important magnetic phenomenon in the thermodynamic limit[16] associated with breaking of the total-spin symmetry. The finite-size magnetic clusters discussed here exhibit a sharply different behavior in this respect. Indeed, as discussed in Ref. 16, the four-site Néel state is the single Slater determinant $|\downarrow\uparrow\downarrow\uparrow\rangle$ (or $|\uparrow\downarrow\uparrow\downarrow\rangle$). It is clear that the total-spin conserving EXD functions $\mathcal{X}_{00}$ (as well as the corresponding Heisenberg eigenvectors) are multideterminantal and have an average spin per localized electron (per site) $\langle S_j^z \rangle = 0$.

We concur with Ref. 16 that the phenomenon of Néel antiferromagnetism is radically modified in assemblies of few electrons. In this section, we argue that instead of "antiferromagnetic ordering" the appropriate physical concept for the WM states found earlier is that of *spin entanglement*. Indeed, in the previous sections, we showed that the EXD wave functions in the regime of Wigner-molecule formation can be approximated as a superposition of a small number of Slater determinants corresponding to well structured spin functions; see, e.g., $\mathcal{X}_{00}^{(1)}$ in Eq. (28). This is a great simplification compared to the initial EXD superposition [Eq. (7)], where the counting index is usually $I \geq 500\,000$. This reduction in the molecular EXD solutions to their equivalent spin functions (described in Sec. V C) (or to the Heisenberg eigenvectors described in Sec. VI) enables one to investigate their properties regarding fundamental quantum behavior associated with quantum correlations and fluctuations beyond the mean field.

The mathematical theory of entanglement is still developing and includes several directions. One way to study entanglement is through the use of properly defined measures of entanglement, e.g., the von Neumann entropy which utilizes the single-particle density matrix. Another way is to catalog and specify classes of entangled states that share common properties regarding multipartite entanglement. A well-known class of N-qubit entangled states are the Dicke states,[34–37] which most often are taken to have the symmetric form

$$\mathcal{X}_{N,k}^{\text{Dicke}} = \binom{N}{k}^{-1/2} (|\underbrace{11\ldots1}_{k}00\ldots0\rangle + \text{Perm}). \tag{63}$$

Each qubit is a linear superposition of two single-particle states denoted by 0 or 1, and the symbol "Perm" stands for all remaining permutations. The 0 or 1 does not have to be necessarily up or down 1/2-spin states. Two-level atoms in linear ultracold traps have already been used as an implementation of a qubit. Dicke states appear in many physical processes such as superradiance and superfluorescence. They can also be realized with photons, where the qubits correspond to the polarization degree of freedom.[37]

In the 1/2-spin case of fermions (e.g., for electrons), the Dicke states of Eq. (63) correspond to a fully symmetric flip of k out of N localized spins. It is apparent that the four-qubit fully polarized ($S=2$ with spin projection $S_z=0$) EXD solution is reproduced by $\mathcal{X}_{20}$ of Eq. (17), and thus it is of the symmetric Dicke form (with $k=2$) displayed above in Eq. (63). On the other part, the DQD EXD states (with $S_z=0$) studied in Sec. V C with $S=0$ and/or $S=1$ represent a natural generalization of Eq. (63) to the class of *asymmetric* Dicke states.

Dicke states with a single flip ($k=1$) are known as W states.[61,62] For $N=4$ electrons, the latter states are related to EXD solutions with $S_z=\pm 1$. For the connection between W states and EXD states for $N=3$ electrons in anisotropic quantum dots, see Ref. 38. W states have already been realized experimentally using two-level ultracold ions in linear traps.[63]

VIII. SUMMARY

Extensive investigations of lateral double quantum dots containing four electrons (*artificial quantum-dot helium molecules*) were performed using the exact-diagonalization method (described in Sec. III), as a function of interdot separation, applied magnetic field, and strength of interelectron repulsion. Different quantum behavior was discovered compared to circular QDs concerning energy spectra, analogies with finite Heisenberg clusters, and aspects of entanglement. It is hoped that the present work will motivate further experimental studies on lateral DQDs with more than two electrons.

Specifically it was found (Sec. V A) that, as a function of the magnetic field, the energy spectra exhibit a low-energy band consisting of a group of six states, and that this number six is not accidental, but a consequence of the conservation of the total spin and of the ensuing spin degeneracies and supermultiplicities expressed in the branching diagram (described in Sec. IV). These six states appear to cross at a single value of the magnetic field and the crossing point gets sharper for larger interdot distances. As the strength of the Coulomb repulsion increases, the six states tend to become degenerate and a well-defined energy gap separates them from the higher-in-energy excited states.

The formation of the low-energy band is a consequence of the localization of the four electrons within each dot (with two electrons on each dot). The result is formation (with increasing strength of the Coulomb repulsion) of a Wigner supermolecule, with the four localized electrons at the corners of a rectangular parallelogram. Using the spin-resolved pair-correlation functions, it was shown that one can map the EXD many-body wave functions to the spin functions associated with four localized spins (Sec. V C).

This mapping led us naturally to studying analogies with finite systems described by model Heisenberg Hamiltonians (referred to often as finite Heisenberg clusters). Specifically, we provided a detailed interpretation of the EXD spin functions and EXD spectra associated with the low-energy band via a four-site finite Heisenberg cluster characterized by two (intradot and interdot) exchange integrals. More importantly, our EXD calculations suggest a prominent oscillatory magnetic-field dependence of the two exchange integrals entering in this four-site Heisenberg Hamiltonian (Sec. VI).

Such strong B dependence of the exchange integrals has been found in previous theoretical and experimental studies in the simpler case of two electrons in quantum dots and it has developed into a central theme in experimental efforts aiming at solid-state implementation of quantum computing. Our EXD results in this paper extend the B dependence of the exchange integrals to larger numbers ($N>2$) of electrons in quantum-dot molecules (see discussion in Sec. VII A). Finally, it was discussed that the EXD spin functions correspond to strongly entangled states known in the literature of quantum information as N-qubit Dicke states (Sec. VII B).

ACKNOWLEDGMENT

This work was supported by the U.S. DOE (Grant No. FG05-86ER45234).

APPENDIX: SINGLE-PARTICLE STATES OF THE TWO-CENTER OSCILLATOR

In this appendix, we discuss briefly the energy spectra associated with the single-particle states of the two-center oscillator Hamiltonian given by Eq. (1). We follow here the notation presented first in Ref. 42. For further details, see Ref. 43.

The calculated two-center oscillator single-particle spectrum for a double quantum dot made of two tunnel-coupled identical QDs (with $\hbar\omega_y=\hbar\omega_{x1}=\hbar\omega_{x2}=3$ meV) plotted versus the distance, d, between the centers of the two dots, is given in Fig. 9. In these calculations, the height of the barrier between the dots varies as a function of d, thus simulating reduced tunnel coupling between them as they are separated; we take the barrier control parameter as $\epsilon_1^b=\epsilon_2^b=0.5$. In the calculations in this appendix, we used GaAs values, $m^*=0.067m_e$ and a dielectric constant $\kappa=12.9$. For the separated single QDs (large d) and the unified QD ($d=0$) limits, the spectra are the same, corresponding to that of a 2D harmonic oscillator (being doubly degenerate for the separated single QDs) with a level degeneracy of $1,2,3,\ldots$. In analogy with real molecules, the single-particle states in the intermediate region ($d>0$) may be interpreted as molecular orbitals (MOs) made of linear superpositions of the states of the two dots comprising the DQ. This qualitative description is intuitively appealing, though it is more appropriate for the weaker coupling regime (large d); nevertheless we continue to use it for the whole range of tunnel-coupling strengths between the dots, including the strong coupling regime where reference to the states of the individual dots is only approximate. Thus, for example, as the two dots approach each other, the lowest levels (n_x,n_y) with $n_x=n_y=0$ on the two dots may combine symmetrically ("bonding") or anti-

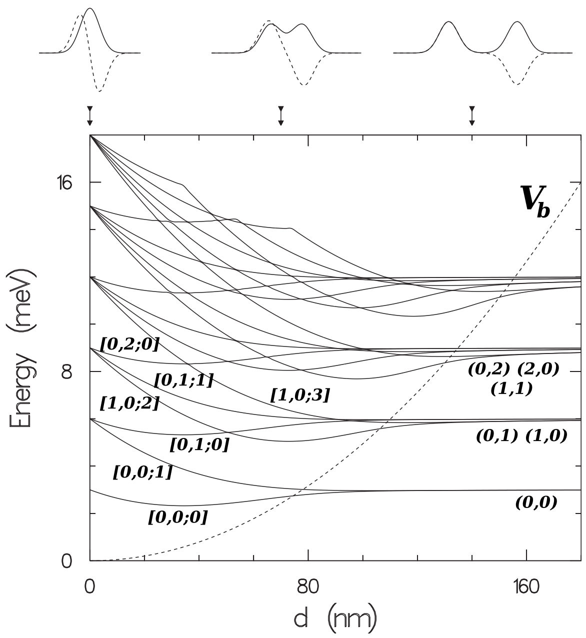

FIG. 9. Single-particle spectra of a double quantum at $B=0$ plotted versus the distance d between two (identical) coupled QDs with a TCO confinement $\hbar\omega_{x1}=\hbar\omega_{x2}=\hbar\omega_y=3$ meV and $h_1=h_2=0$ [see Eq. (1)]. For all d's the barrier control parameters were taken as $\epsilon_1^b=\epsilon_2^b=0.5$, i.e., the barrier height (depicted by the dashed line) varies as $V_b(d)=V_0(d)/2$. Molecular orbitals correlating the united ($V_b=0$) and separated-dots limits are denoted along with the corresponding (on the right) single-QD states. Wave function cuts at $y=0$ along the x axis at several distances d (see arrows) corresponding to the lowest bonding and antibonding eigenvalues (solid and dashed lines, respectively) are displayed at the top. Energies in meV and distances in nm.

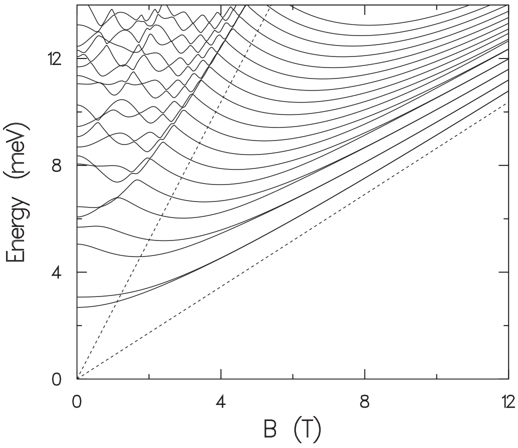

FIG. 10. Single-particle spectrum of the $d=70$ nm ($\hbar\omega_{x1}=\hbar\omega_{x2}=\hbar\omega_y=3$ meV, $V_b=2.43$ meV, $h_1=h_2=0$) double quantum dot versus B (in T). The $\hbar\omega_c/2$ ($\mathcal{N}_L=0$, lower line) and $3\hbar\omega_c/2$ ($\mathcal{N}_L=1$, upper line) first and second Landau levels are given by the dashed lines.

symmetrically ("antibonding") to form [0,0;0] and [0,0;1] MOs, with the third index denoting the total number of nodes of the MO along the interdot axis (x), that is, $2n_x+\mathcal{I}$, $\mathcal{I}=0$ or 1; for symmetric combinations ($\mathcal{I}=0$), this index is even and for antisymmetric ones ($\mathcal{I}=1$), it is odd. Between the separated-single-QDs and the unified-QD limits, the degeneracies of the individual dots' states are lifted, and in correlating these two limits the number of x nodes is conserved; for example the [0,0;1] MO converts in the unified-QD limit into the (1,0) state of a single QD, the [1,0;2] MO into the (2,0) state, and the [0,1;1] MO into the (1,1) state (see Fig. 9). Note that MOs of different symmetries may cross, while they do not if they are of the same symmetry.

In a magnetic field, the TCO model constitutes a generalization of the Darwin-Fock model[64] for noninteracting electrons in a single circular QD. The single-particle spectra for the DQD ($d=70$ nm, $V_b=2.43$ meV) in a magnetic field (B) are shown in Fig. 10 (here we neglect the Zeeman interaction which is small for our range of B values with $g^*=-0.44$ for GaAs). The main features are the following: (i) the multiple crossings (and avoided crossings) as B increases, (ii) the decrease in the energy gap between levels, occurring in pairs (such as the lowest bonding-antibonding pair), portraying an effective reduced tunnel coupling between the QDs comprising the DQD as B increases, and (iii) the "condensation" of the spectrum into the sequence of Landau levels $(\mathcal{N}_L+1/2)\hbar\omega_c$, $\mathcal{N}_L=0,1,2,\ldots$ (the $\mathcal{N}_L=0$ and $\mathcal{N}_L=1$ bands are depicted, respectively, by the lower and upper dashed lines in Fig. 10). This is similar to the behavior of the single-particle Darwin-Fock spectrum for harmonically confined electrons in a circular QD (Ref. 64) (note, however, that the geometry of the DQD is noncircular and deviates from a simple harmonic confinement).

---

[*] constantine.yannouleas@physics.gatech.edu
[†] uzi.landman@physics.gatech.edu

[1] L. P. Kouwenhoven, D. G. Austing, and S. Tarucha, Rep. Prog. Phys. **64**, 701 (2001).
[2] R. Hanson, L. P. Kouwenhoven, J. R. Petta, S. Tarucha, and L. M. K. Vandersypen, Rev. Mod. Phys. **79**, 1217 (2007).
[3] P. A. Maksym, H. Imamura, G. P. Mallon, and H. Aoki, J. Phys.: Condens. Matter **12**, R299 (2000).
[4] S. M. Reimann and M. Manninen, Rev. Mod. Phys. **74**, 1283 (2002).
[5] C. Yannouleas and U. Landman, Rep. Prog. Phys. **70**, 2067 (2007).
[6] D. Loss and D. P. DiVincenzo, Phys. Rev. A **57**, 120 (1998).
[7] G. Burkard, D. Loss, and D. P. DiVincenzo, Phys. Rev. B **59**, 2070 (1999); G. Burkard, G. Seelig, and D. Loss, *ibid.* **62**, 2581 (2000).
[8] I. Žutić, J. Fabian, and S. Das Sarma, Rev. Mod. Phys. **76**, 323 (2004).
[9] D. D. Awschalom and M. E. Flatté, Nat. Phys. **3**, 153 (2007).
[10] R. Woodworth, A. Mizel, and D. A. Lidar, J. Phys.: Condens. Matter **18**, S721 (2006).
[11] S. Tarucha, D. G. Austing, T. Honda, R. J. van der Hage, and L.

P. Kouwenhoven, Phys. Rev. Lett. **77**, 3613 (1996).

[12] M. Ciorga, A. S. Sachrajda, P. Hawrylak, C. Gould, P. Zawadzki, S. Jullian, Y. Feng, and Z. Wasilewski, Phys. Rev. B **61**, R16315 (2000).

[13] M. Avinun-Kalish, M. Heiblum, O. Zarchin, D. Mahalu, and V. Umansky, Nature (London) **436**, 529 (2005).

[14] P. V. Hendriksen, S. Linderoth, and P. A. Lindgård, Phys. Rev. B **48**, 7259 (1993).

[15] S. Haas, in *Lectures on the Physics of Strongly Correlated Systems XII*, edited by A. Avella and F. Mancini, AIP Conf. Proc. No. 1014 (AIP, Melville, NY, 2008).

[16] P. Fazekas, *Lecture Notes on Electron Correlation and Magnetism* (World Scientific, Singapore, 1999).

[17] M. B. Tavernier, E. Anisimovas, F. M. Peeters, B. Szafran, J. Adamowski, and S. Bednarek, Phys. Rev. B **68**, 205305 (2003).

[18] M. Rontani, C. Cavazzoni, D. Bellucci, and G. Goldoni, J. Chem. Phys. **124**, 124102 (2006).

[19] A. Ghosal, A. D. Güclü, C. J. Umrigar, D. Ullmo, and H. U. Baranger, Phys. Rev. B **76**, 085341 (2007).

[20] Since each natural He atom is a closed-shell system, the natural helium molecule (He_2) is unstable according to the traditional theory of covalent chemical bonding [R. S. Mulliken, Proc. Nat. Acad. Sci. **12**, 158 (1926)]; the natural He_2 is a weakly bound giant-in-length molecule and was recently produced at ultracold temperatures [J. Léonard, M. Walhout, A. P. Mosk, T. Müller, M. Leduc, and C. Cohen-Tannoudji, Phys. Rev. Lett. **91**, 073203 (2003)];since the electronic structure of the four-electron DQD described in this paper exhibits analogies to finite Heisenberg clusters, we stress that it is drastically different from that associated with covalent bonding in natural molecules.

[21] M. Helle, A. Harju, and R. M. Nieminen, Phys. Rev. B **72**, 205329 (2005).

[22] L. X. Zhang, D. V. Melnikov, and J. P. Leburton, Phys. Rev. B **74**, 205306 (2006).

[23] H. Chan, P. Fallahi, A. Vidan, R. M. Westervelt, M. Hanson, and A. C. Gossard, Nanotechnology **15**, 609 (2004).

[24] T. Hatano, S. Amaha, T. Kubo, Y. Tokura, Y. Nishi, Y. Hirayama, and S. Tarucha, Phys. Rev. B **77**, 241301(R) (2008).

[25] B. Szafran and F. M. Peeters, Phys. Rev. B **71**, 245314 (2005).

[26] T. Chwiej and B. Szafran, Phys. Rev. B **78**, 245306 (2008).

[27] R. Pauncz, *The Construction of Spin Eigenfunctions: An Exercise Book* (Kluwer Academic/Plenum Publishers, New York, 2000).

[28] C. Yannouleas and U. Landman, Phys. Rev. Lett. **82**, 5325 (1999); **85**, 2220 (2000).

[29] C. Yannouleas and U. Landman, J. Phys.: Condens. Matter **14**, L591 (2002).

[30] C. Yannouleas and U. Landman, Int. J. Quantum Chem. **90**, 699 (2002).

[31] C. Ellenberger, T. Ihn, C. Yannouleas, U. Landman, K. Ensslin, D. C. Driscoll, and A. C. Gossard, Phys. Rev. Lett. **96**, 126806 (2006).

[32] T. Ihn, C. Ellenberger, K. Ensslin, C. Yannouleas, U. Landman, D. C. Driscoll, and A. C. Gossard, Int. J. Mod. Phys. B **21**, 1316 (2007).

[33] D. M. Zumbühl, C. M. Marcus, M. P. Hanson, and A. C. Gossard, Phys. Rev. Lett. **93**, 256801 (2004).

[34] R. H. Dicke, Phys. Rev. **93**, 99 (1954).

[35] F. Verstraete, J. Dehaene, B. De Moor, and H. Verschelde, Phys. Rev. A **65**, 052112 (2002).

[36] J. K. Stockton, J. M. Geremia, A. C. Doherty, and H. Mabuchi, Phys. Rev. A **67**, 022112 (2003).

[37] J. K. Korbicz, O. Gühne, M. Lewenstein, H. Häffner, C. F. Roos, and R. Blatt, Phys. Rev. A **74**, 052319 (2006).

[38] Yuesong Li, C. Yannouleas, and U. Landman, Phys. Rev. B **76**, 245310 (2007).

[39] A three-dimensional magnetic-field-free version of the TCO has been used in the description of fission in metal clusters (Ref. 40) and atomic nuclei (Ref. 41).

[40] C. Yannouleas and U. Landman, J. Phys. Chem. **99**, 14577 (1995); C. Yannouleas, R. N. Barnett, and U. Landman, Comments At. Mol. Phys. **31**, 445 (1995).

[41] J. Maruhn and W. Greiner, Z. Phys. **251**, 431 (1972); C. Y. Wong, Phys. Lett. B **30**, 61 (1969).

[42] R. N. Barnett, C. L. Cleveland, H. Häkkinen, W. D. Luedtke, C. Yannouleas, and U. Landman, Eur. Phys. J. D **9**, 95 (1999).

[43] The two-dimensional TCO was used earlier to approximate the solutions of the many-body Hamiltonian in Eq. (4) at the level of unrestricted Hartree-Fock exhibiting breaking of total-spin symmetry; see Refs. 28–30. For a review of the necessary subsequent step of symmetry restoration, see Ref. 5.

[44] Due to the very long CPU times required for calculating surfaces, several CPDs at $B=0$ were calculated using $K=32$. We checked that this does not influence our analysis of spin functions compared to $K=50$.

[45] R. B. Lehoucq, D. C. Sorensen, and C. Yang, *ARPACK Users' Guide: Solution of Large-Scale Eigenvalue Problems with Implicitly Restarted Arnoldi Methods* (SIAM, Philadelphia, 1998).

[46] A. Szabo and N. S. Ostlund, *Modern Quantum Chemistry* (McGraw-Hill, New York, 1989).

[47] For the expression $\mathcal{X}_{00}$ in Eq. (15), see Y. Suzuki and K. Varga, *Stochastic Variational Approach to Quantum-Mechanical Few-Body Problems* (Springer, Berlin, 1998), Chap. 6.6; for the remaining two expressions for $S_z=0$, i.e., $\mathcal{X}_{10}$ and $\mathcal{X}_{20}$ [Eqs. (16) and (17), respectively], see Ying Li, Ph.D. dissertation, Georgia Institute of Technology, 2009 (http://hdl.handle.net/1853/28186).

[48] A careful inspection of Figs. 3(a) and 3(b) shows that the curves for the two $P_{xy}=1$, $S=0$ states in the low-energy band do *not* actually cross. This anticrossing property is also discussed in Sec. IV (which compares the CPDs of these two states at $B=0$ and $B=2$ T) and in Sec. VI (which analyzes the eigenenergies of the four-site Heisenberg Hamiltonian).

[49] C. Yannouleas and U. Landman, Phys. Rev. B **69**, 113306 (2004).

[50] C. Yannouleas and U. Landman, Phys. Rev. Lett. **85**, 1726 (2000).

[51] V. A. Schweigert and F. M. Peeters, Phys. Rev. B **51**, 7700 (1995).

[52] M. R. Geller and G. Vignale, Phys. Rev. B **53**, 6979 (1996).

[53] E. Manousakis, Rev. Mod. Phys. **63**, 1 (1991).

[54] J. S. Meyer and K. A. Matveev, J. Phys.: Condens. Matter **21**, 023203 (2009).

[55] C. Shi, G. S. Jeon, and J. K. Jain, Phys. Rev. B **75**, 165302 (2007).

[56] Ph. Anderson, Phys. Today **61** (4), 8 (2008).

[57] V. J. Emery, Phys. Rev. B **14**, 2989 (1976).

[58] See review by S. Viefers, P. Koskinen, P. Singha Deo, and M. Manninen, Physica E **21**, 1 (2004).

[59] D. Sen and R. Chitra, Phys. Rev. B **51**, 1922 (1995).

[60] D. S. Rokhsar, Phys. Rev. Lett. **65**, 1506 (1990); J. K. Freericks, L. M. Falicov, and D. S. Rokhsar, Phys. Rev. B **44**, 1458 (1991).

[61] W. Dür, G. Vidal, and J. I. Cirac, Phys. Rev. A **62**, 062314 (2000).

[62] V. Coffman, J. Kundu, and W. K. Wootters, Phys. Rev. A **61**, 052306 (2000).

[63] H. Häffner, W. Hänsel, C. F. Roos, J. Benhelm, D. Chek-al-kar, M. Chwalla, T. Körber, U. D. Rapol, M. Riebe, P. O. Schmidt, C. Becher, O. Gühne, W. Dür, and R. Blatt, Nature (London) **438**, 643 (2005).

[64] V. Fock, Z. Phys. **47**, 446 (1928); C. G. Darwin, Proc. Camb. Philos. Soc. **27**, 86 (1930).